Linewidth Reduction of a Diode Laser by Optical Feedback for Strontium BEC Applications

master thesis in physics

by

Bo HUANG

submitted to the Faculty of Mathematics, Computer Science and Physics of the University of Innsbruck

in partial fulfillment of the requirements for the degree of Master of Science

Supervisors:
Rudolf Grimm, Institut für Experimentalphysik
Florian Schreck, IQOQI, Österreichische Akademie der Wissenschaften

Innsbruck, November 2009

Table of Contents

Abstract

We present a diode-based laser design with a linewidth of 2 kHz. This laser is locked to the ${}^1S_0 - {}^3P_1$ transition of strontium at 689 nm. Light from a semiconductor source is filtered by a temperature stabilized and vibration isolated high finesse cavity, then fed back to the diode for linewidth reduction. A Pound-Drever-Hall technique and a loop phase adjusting mirror are used to achieve a tighter and more stable locking. The theory of this optical feedback technique is discussed.

To lock the laser to the Sr ${}^1S_0 - {}^3P_1$ transition, we stabilize the cavity length via saturation spectroscopy on a heated strontium gas pipe. An offset of dispersive error signal caused by amplitude modulation of the light is canceled by a reference signal before the spectroscopy. Estimated from the close loop error signal, this laser achieves a linewidth less than 2 kHz and a long-term stability of about 10 kHz. This laser system is easy to setup and requires only low bandwidth electronics and a simple diode laser without grating stabilization.

Using this laser, our group cooled strontium atoms down to 2.5 μK and recently achieved the Bose-Einstein condensation of ^{84}Sr.

Acknowledgements

I would like to thank my supervisors Florian Schreck and Rudi Grimm. Thank you for your guidance in this project as well as warm encouragements and helps. I am also thankful to Simon Stellmer, who gave me a warm hand at the beginning of this project and continued with his kind suggestions.

Meng Khoon Tey and I had been 'fighting' together continuously in the lab for months. He taught and helped me with great patience and generosity in a way of brotherhood. I can never forget the stars and dawns we saw when we came out from the lab.

Thank you also to everyone in our neighboring lab, Andreas Trenkwalder, Devang S. Naik, Frederik Spiegelhalder and Eric Wille. From time to time you came to me with nice suggestions and immediate help.

Many thanks to Gerhard Hendl, Andreas Strasser and Stefan Haslwanter. Only with your excellent electronic and mechanic works could this project be done smoothly.

Many good friends of mine, especially my former roommate Leonid Sidorenkov and many of my university classmates, supported me heartfully either in physics or my life. I greatly appreciate your friendship.

Finally, I am full of gratitude to my parents and my girlfriend Weier. You filled me with love and I miss you so much.

Bo HUANG

Innsbruck, Austria
October 1, 2009

Chapter 1

Introduction

Ultracold gases of strontium have been attracting attention for many reasons. Ultra-precise optical lattice clocks using either ^{87}Sr or ^{88}Sr have been realized [1, 2]. Many schemes for quantum computation [3, 4], simulations of quantum many-body phenomena [5], and the formation of ultracold Sr_2 molecules [6, 7] are also of considerable interest.

Most of these applications rely on the two valence electrons of strontium and their singlet and triplet spin states. Transitions between singlet and triplet states are spin forbidden and very narrow. Such narrow lines can be used for optical clocks, quantum computation ($^1S_0 - ^3P_0$), narrow line trapping and cooling by using a Magneto-Optical Trap (MOT) ($^1S_0 - ^3P_1$) and meta-stable state trapping ($^1S_0 - ^3P_2$) [8]. Besides these benefits, the bosonic isotopes of Sr have zero nuclear spin so they are scalar particles in the $J = 0$ state, which is useful in optical metrology and quantum sensors [9].

For dilute ultracold atoms, quantum degeneracy is an important criterion for low temperature and high phase density. Since the first Bose-Einstein Condensation (BEC) of dilute ultracold rubidium atoms was achieved, many other atomic species have also been cooled to degeneracy - either by forming BECs [1] or fermionic degenerate states [12]. Recently, our group achieve the BEC of strontium for the first time [8].

To obtain the Sr BEC, a second stage MOT is operated on the Sr $^1S_0 - ^3P_1$ intercombination transition, which is at 689 nm with a natural linewidth of 7.4 kHz. In this stage, a very stable laser source narrower than 7.4 kHz at the transition frequency is needed to minimize the atomic temperature. In this thesis, we will discuss how to set up such a laser source and theoretically analyze the performance of this laser. In chapter 2, the theory of linewidth reduction of a semiconductor laser by optical feedback is discussed; in chapter 3, we present the design and alignment procedure of our laser setup; in chapter 4, the publication [8] on our ^{84}Sr BEC experiment is given; finally, details and experiences of the laser setup are listed in the appendix.

[1] For BEC, except the recent ^{40}Ca BEC in [10], a nice list can be found in [11].

Chapter 2

Linewidth Reduction of a Semiconductor Laser by Optical Feedback

2.1 Using Diode Lasers

When investigating the interaction between atoms and light, a reliable laser that can be tuned to a desired atomic transition is necessary. Decades ago, a tunable dye laser [1] was the first choice, but now the steadily improving semiconductor lasers have dominated this market. Diode lasers [13, 14, 15] can be easily tuned by changing its temperature and driving current, and are relatively cheap and compact. Although the tunable range of a single diode laser is only a few ten nanometers, different types of diodes cover most of the wavelength from ultraviolet to infrared. Furthermore, the linewidth of a diode laser can be reduced by electrical or optical feedbacks to even sub-Hz level [16]. Laser diodes can also be used easily to amplify laser power via injection-locking. Because of these merits, diode lasers have been the most popular laser source for cold atom researches, such as laser cooling and trapping of atoms, optical clocks, high resolution laser spectroscopy and quantum computation.

However, direct applications of free running diode lasers are limited for various reasons. First, typical linewidth of a free running diode laser is 10 to 20 MHz, which is usually much larger than the linewidth of the studied atomic transition. Second, the output frequency of a free running diode laser cannot be tuned continuously by temperature and driving current and the tunable range is also limited. Currently, the most popular technique to achieve a narrow linewidth diode laser and increase its frequency tunability is the so called External Cavity Diode Laser (ECDL) [15]. In this technique, a grating is used to feed part of the light back to the diode so that the laser frequency is also selected by the grating and the cavity formed between the grating and the back end of the diode. By adjusting the position and angle of the grating,

[1] Page 601, [13]

we can tune the laser frequency in a larger and more continuous range. At the same time, the laser linewidth is reduced to about 500 kHz [15, 17]. Further linewidth reduction of an ECDL can be done by electrical feedback. In such a system, a well-isolated high-finesse Fabry Pérot Interferometer (FPI), which serves as a frequency discriminator, and a very quiet electrical feedback system with high gain and wide bandwidth are needed.

An alternative way for linewidth reduction is by using weak optical feedback from an external cavity [15]. This technique is much less demanding in electronics and less time consuming in setting up. On the other hand, such weak optical feedback cannot improve the tunability of the laser frequency. That means we have to first find a 'good' diode which can lase stably at the wanted frequency, then we can only fine-tune its frequency and reduce its linewidth. For the laser diode we used (HL6738MG, 690nm, 35 mW), we typically tried 10 diodes to find such a 'good' one.

2.2 Reference Cavity and Electrical Feedback Locking Schemes

A stable high-finesse cavity is important in both electrical feedback and optical feedback locking schemes. The basic concepts of a FPI can be found in many textbooks [18] covering laser principles. One thing to emphasize is that usual analysis of light transmitted through or reflected from a cavity is valid only for a steady-state - which means the laser frequency fluctuation should be so slow that a steady-state can be established in the cavity. If the the laser or cavity is fluctuating too fast to reach an equilibrium, these treatments are no longer valid. For example, in the steady-state case, the reflected light of a cavity could never be stronger than the incident light. However, due to a rapid phase fluctuation of the incoming light, the reflected light may interfere constructively with the outgoing field from the cavity. In this case, an interference enhanced reflection above incoming light power is observable near the cavity resonance. Analysis of cavity's response to such high frequency noises can be found in [19].

Using a cavity or an atomic or molecular transition as a frequency reference, there are many ways to stabilize laser frequency by electrical feedback. Generally, these locking schemes can be divided into two categories: intensity discrimination or interferometry based. The former one monitors the power of a probe light, e.g. transmission through a cavity or saturation spectroscopy. The later uses two (or more) modes in the probe light and generates an error signal via beating or split-detection of the modes [2]. One of the most popular frequency locking techniques is the Pound-Drever-Hall (PDH) technique [21, 22], which is based on interferometry and has a high speed response even when the fluctuation frequency is too high to be

[2] A short but nice discussion is in the first part of [20]. Details could be found in references of that article or other textbooks.

described by a steady-state [19]. In our experiment, this technique is used to assist optical feedback locking.

For the electrical feedback system used in a PDH scheme, general discussions about how to design, analyze and optimize a servo system could be found in control theory textbooks [23] and reviews such as [24] and [25].

2.3 Linewidth Reduction by Optical Feedback

It has been shown both experimentally and theoretically that optical feedback from a high-finesse external cavity can reduce the linewidth of a diode laser significantly [26, 27, 28]. An earlier report [28] shows that a static frequency noise power reduction of 50-60 dB is possible using this technique. Here an intuitive steady-state analysis will be discussed to explain the nature of this technique and to estimate the linewidth reduction in our design.

2.3.1 The Field Equation and Its Steady-State Solution

A simplified optical feedback scheme is illustrated in figure 2.1. Part of the light from a laser diode passes through a high-finesse cavity, then the transmitted light is coupled back to the diode. To the intra-diode light field which is leaking from the diode to give the output light, the feedback light could be treated as a leaking-compensation or a driving field. When the feedback is very week, a small leaking-compensation term can be added to the field equations of a free running diode laser to describe the new system. Quantitatively, the performance of this system depends on several parameters:

1. The free-running laser frequency ω_{N}. Since the gain spectral width is much larger than the separation of longitude modes of the diode, ω_{N} is mainly determined by the diode cavity mode locates nearest to center of the gain curve.

$$\omega_{\mathrm{N}} \simeq N \frac{c}{2 n_{\mathrm{LD}} l_{\mathrm{LD}}}, \tag{2.3.1}$$

where l_{LD} is the physical length of the diode cavity and N denotes the Nth longitudinal mode of the diode. The refractive index n_{LD} depends on the temperature and driving current of the diode.

2. The feedback delay time τ_f. It is obtained by dividing the length of the optical feedback loop (including external cavity length) by the speed of light. In the following discussion, we also convert it to a delay phase and use only the fractional part ϕ_f defined by

$$\omega \tau_f = 2\pi j_f + \phi_f, \tag{2.3.2}$$

where $j_f \in \mathbb{Z}$, $\phi_f \in [0, 2\pi)$ and ω is the actual frequency of the laser under external feedback.

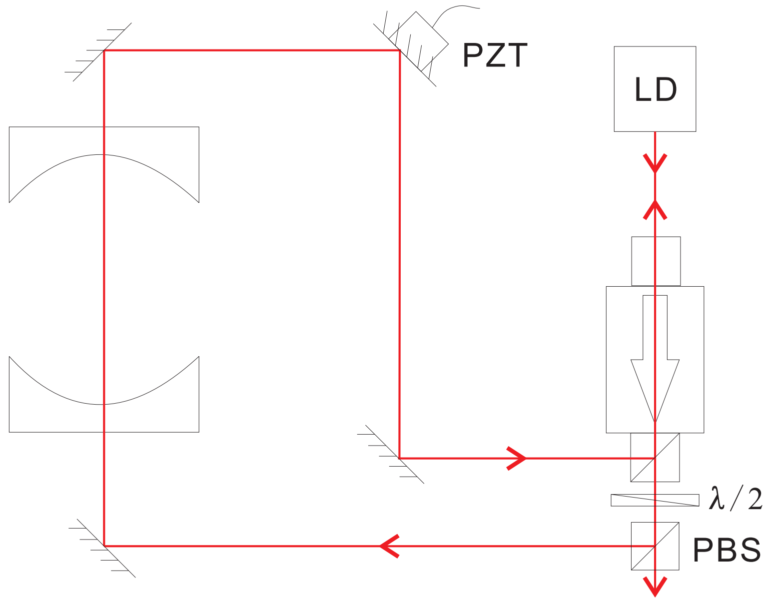

Figure 2.1: Schematic setup of our optical feedback system. Light from the laser diode (LD) passes a Faraday isolator and a high-finesse cavity. The transmitted light is fed back to the diode. Feedback loop length is controlled by a mirror driven by a Piezoelectric Transducer (PZT).

3. The light round-trip time in the external resonator, τ_c. Similarly, we define a residual delay phase ϕ_c by

$$\omega\tau_c = 2\pi j_c + \phi_c. \tag{2.3.3}$$

4. The reflectivity R of the mirrors forming the external cavity. The transfer function of the external cavity, playing the role of a filter, is given by

$$g(\omega) = \frac{1-R}{1-Re^{i\omega\tau_c}}. \tag{2.3.4}$$

An overall phase of $e^{-i\omega\tau_c/2}$ caused by the length of the cavity is omitted because it has been included in τ_f.

5. The feedback level describing 'how much light' is used in optical feedback is given as

$$\gamma = \left|\frac{E_{\mathrm{f0}}}{E_{\mathrm{out}}}\right|, \tag{2.3.5}$$

where E_{out} is the field amplitude of output light from laser diode and E_{f0} is that of the feedback light not filtered by an ideal cavity. It accounts for the total field attenuation of the feedback loop except for the effect described by the transfer function $g(\omega)$.

6.The leaking compensation rate of the laser diode

$$\rho = \frac{1-R_{\mathrm{LD}}}{\tau_{\mathrm{LD}}\sqrt{R_{\mathrm{LD}}}}. \tag{2.3.6}$$

It involves the reflectivity of the diode output facet R_{LD}, and the diode cavity round trip time $\tau_{\mathrm{LD}} = 2n_{\mathrm{LD}}l_{\mathrm{LD}}/c$. The leaking compensation effect caused by a weak optical feedback can be equivalent to a small increase of R_{LD}. Ignoring multiple round trips in the feedback loop in the case of weak feedback, $\rho\gamma g(\omega)$ is the first order term of the leaking compensation, see the appendix of [26] for details. ρ and ω_{N} can be related by (eliminating n_{LD})

$$\rho = \frac{\rho_0}{\omega_{\mathrm{N0}}}\omega_{\mathrm{N}} = \kappa\omega_{\mathrm{N}}, \tag{2.3.7}$$

where constant $\kappa = \rho_0/\omega_{\mathrm{N0}}$ can be calculated from any steady-state.

7. The linewidth broadening factor α, which is the ratio of the real part and imaginary part of the refractive index, $n = \chi' + i\chi''$, in the steady-state,

$$\alpha = \frac{\Delta\chi'}{\Delta\chi''}. \tag{2.3.8}$$

For convenience, we use an equivalent parameter $\theta = \tan^{-1}\alpha$ in our calculation.

8. The gain rate deviation from the steady-state of a free running laser due to optical feedback, ΔG. It is the gain rate of the active material subtracted by the loss rate coming from absorption and diode cavity leaks.

Finally, if we neglect spontaneous emission and assume a single mode laser with instantaneous gain-media response and slowly varying envelope, the evolution of the intra-cavity electric field with a weak feedback can be described by the extended field equation [27]

$$\frac{d}{dt}E(t) = [-i\omega_{\mathrm{N}} + \frac{\Delta G}{2}(1 - i\alpha)]E(t) + \rho\gamma g(\omega)E(t - \tau_f). \tag{2.3.9}$$

The first term on the right-hand side describes the steady-state evolution of the N*th* longitude eigen-mode of a free-running laser, all other terms are perturbations. The $\Delta GE(t)/2$ term amplifies the field by the deviation of gain rate ΔG. An extra phase $-i\alpha\Delta GE(t)/2$, coming from the gain effect, is determined by the imaginary part of the refractive index. And $\rho\gamma g(\omega)E(t - \tau_f)$ is the leaking compensation term.

For a dynamic analysis, another equation is needed to give the relation between $E(t)$, ΔG and the carrier population N_e. However, only (2.3.9) is enough to give a steady-state solution of the electric field.

We assume a steady-state solution of (2.3.9)

$$E(t) = E_0 e^{-i\omega t}. \tag{2.3.10}$$

Taking (2.3.10) into (2.3.9) and separating the complex equation into the real part and the imaginary part, we will have

$$\omega = \omega_{\mathrm{N}} + \omega_{\mathrm{N}}\frac{A}{X}[R\sin(\theta + \phi_f - \phi_c) - \sin(\theta + \phi_f)] \tag{2.3.11}$$

$$\Delta G = \omega_{\mathrm{N}}\frac{2A}{X\sqrt{1+\alpha^2}}[R\cos(\phi_f - \phi_c) - \cos(\phi_f)], \tag{2.3.12}$$

where

$$A = \frac{\gamma \cdot \kappa \cdot (1-R)}{\cos\theta} \tag{2.3.13}$$
$$X = 1 + R^2 - 2R\cos(\phi_c) \tag{2.3.14}$$

From result (2.3.11), we can define the frequency fluctuation suppression ratio

$$\eta = \frac{\partial \omega}{\partial \omega_{\mathrm{N}}} = \frac{\partial f}{\partial f_{\mathrm{N}}} \tag{2.3.15}$$

If η is very small, frequency fluctuation caused by the fluctuation of ω_{N} is significantly suppressed.

To have an intuitive picture of solution (2.3.11), we rearrange it to get

$$\omega_{\mathrm{N}} = \frac{\omega}{1 + A\frac{R\sin(\theta+\phi_f-\omega\tau_c)-\sin(\theta+\phi_f)}{1+R^2-2R\cos(\omega\tau_c)}} \tag{2.3.16}$$

where only ω_{N}, ω and ϕ_f are not fixed. We then adopt the following set of typical values for numerical calculations [3].

$$\begin{aligned}
\omega_{\mathrm{N}0} &= 2\pi \times 434.829 \text{ THz} \\
\tau_c &= 6.67 \times 10^{-10} \text{ s} \\
R &= 0.9998 \\
\gamma &= 0.01 \\
\rho_0 &= 2.5 \times 10^{11} \text{ s}^{-1} \\
\alpha &= 5
\end{aligned}$$

First, straight forward solutions when $\phi_f + \theta = 0$ are plotted in figure 2.2. Since dynamics of small variations to the result of (2.3.9) requires $\eta > 0$ for a stable steady-state solution [28], only segments with positive slope in figure 2.2 are stable solutions .

In the left panel of figure 2.2, since A in (2.3.16) is very small, the curve of $f = \omega/2\pi$ (blue) is close to that of $f = f_{\mathrm{N}} = \omega_{\mathrm{N}}/2\pi$ (black) for most values of f_{N}, except for sharp dispersion features (they are so sharp that they look like horizontal lines in the left panel) at the resonances of the external cavity. These features come from $1 + R^2 - 2R\cos(\omega\tau_c)$ in (2.3.16). A small positive $\eta = \partial f/\partial f_{\mathrm{N}}$ suppresses frequency fluctuations caused by f_{N}. The amplitude of dispersion in f_{N} gives frequency capture range of this laser.

The right panel of figure 2.2 shows the zoom-in of one of these dispersions. It is illustrated that the dispersion has a width in f roughly equals to the Full-Width-of-Half-Maximum of the external cavity transmission ($\mathrm{FWHM_x}$). Different curves show

[3] Parameters of our external cavity, laser wavelength and feedback level are used. Other details can be found in [27] and [28].

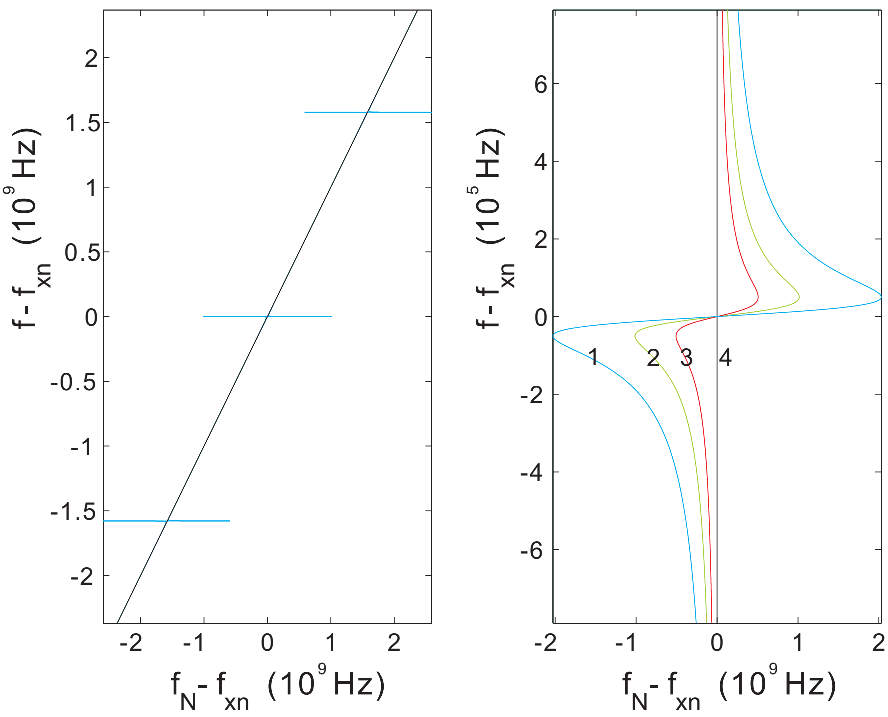

Figure 2.2: f is the actual laser frequency with feedback, f_{N} is the free-running laser frequency and f_{xn} is the nth resonant frequency of the external cavity. In both panels, $\phi_f = -\theta$. Left panel: three sharp dispersion features, which are so narrow compared to the FSR of the external cavity that they look like horizontal lines, appear when f is at $f_{\mathrm{x(n\text{-}1)}}$, f_{xn} and $f_{\mathrm{x(n+1)}}$ respectively. The external cavity has a FSR of 1.58 GHz and a finesse of 1.57×10^4. Feedback level is set at $\gamma = 1\times10^{-2}$. A black line shows $f = f_{\mathrm{N}}$ for reference. Right panel: zoom-in of dispersion features are shown. The first three curves correspond to different feedback levels: $\gamma_1 = 2\times10^{-2}$, $\gamma_2 = 1\times10^{-2}$ and $\gamma_3 = 5\times10^{-3}$ while the black line 4 shows $f = f_{\mathrm{N}}$. A larger amplitude of the dispersion curve in f_{N} means a larger capture range. A small $\eta = \partial f/\partial f_{\mathrm{N}}$ less than 10^{-4} implies a significantly reduced linewidth.

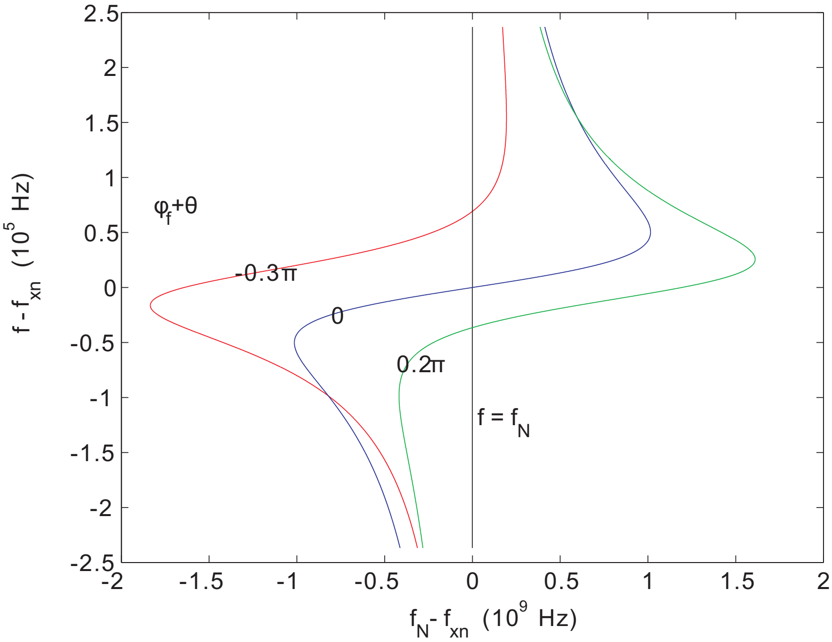

Figure 2.3: Laser frequency f can be tuned to the n*th* external cavity resonance f_{xn} by changing the feedback loop phase ϕ_f at a given free running frequency f_{N}. At the locking points where $f - f_{\mathrm{xn}} = 0$, η is minimized (noise suppression maximized) if $f_{\mathrm{N}} = f_{\mathrm{xn}}$ (corresponds to $\phi_f + \theta = 0$).

that a higher feedback level γ corresponds to a stronger linewidth reduction and an increased 'capture range'. However, if γ is too large, capture ranges can be larger than the FSR of the external cavity, and capture ranges of nearing cavity resonances begin to overlap. The laser might be unstable in the overlapped regions.

The effect of different optical feedback phase ϕ_f is shown in figure 2.3. ϕ_f can shift f at a given f_{N}. We use the PDH technique to control ϕ_f, i.e. by sending the PDH error signal to a PZT to control the feedback path length, so that f can be locked to the center of the n*th* resonance of the external cavity, f_{xn}.

2.3.2 Estimated Frequency Fluctuation Suppression Ratio and Capture Ranges

After understanding the nature of weak optical feedback from an external cavity, we can estimate quantitatively the performance of our system. The frequency capture range of our setup can be estimated via the amplitude (in f_{N}) of the dispersion feature shown in figure 2.2. Adopting approximations that A and (1-R) are very small in (2.3.16), we can get the full capture range (FCR) as

$$\mathrm{FCR} = \frac{Af}{1-R} = \frac{\gamma\rho_0}{2\pi\cos\theta}. \tag{2.3.17}$$

It shows that FCR is proportional to the feedback level γ in the weak feedback regime. In our system, FCR $= 203$ GHz $\times\,\gamma$. FCR should be smaller than 1.5 GHz to prevent mode hopping. Equation (2.3.17) also provides us a way to estimate noise suppression ratio η simply by

$$\mathrm{FWHM_x/FCR} = \frac{2(1-R)\cos\theta}{\gamma\rho_0}\mathrm{FSR_x}, \tag{2.3.18}$$

where $\mathrm{FSR_x}$ is the FSR of the external cavity. (2.3.18) is about twice of the minimal suppression ratio η. For the maximum feedback level γ such that FCR $= \mathrm{FSR_x}$, this estimation gives $\eta = 1/F$, where F is the finesse of the external cavity.

A more precise solution of minimal η (when $\phi_f + \theta = 0$ and $\omega_c\tau_c = 2\pi N$) as a function of γ is

$$\eta = \frac{\partial f}{\partial f_\mathrm{N}} = \left[\frac{\partial \omega_\mathrm{N}}{\partial \omega}\right]^{-1} = \frac{1}{1+\frac{\gamma\rho_0}{(1-R)\mathrm{FSR_x}\cos\theta}}. \tag{2.3.19}$$

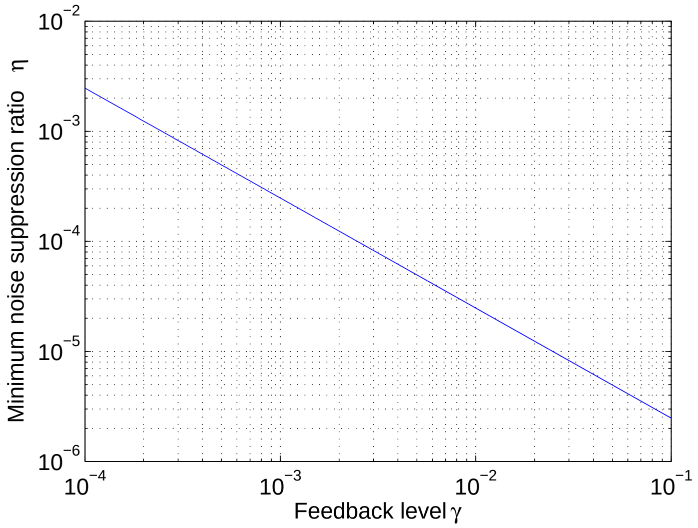

Figure 2.4: Minimum η as a function of feedback level γ, corresponds to $\phi_f + \theta = 0$ and $\omega_c\tau_c = 2\pi N$.

Figure 2.4 shows η as a function of γ, this curve is calculated under the condition that [4] $\phi_f + \theta = 0$ and $\omega_c\tau_c = 2\pi N$. Since our free-running laser has a linewidth of about 15 MHz, the reduced linewidth could be less than 1 kHz when γ is larger than 0.004.

However, only optical feedback cannot compensate slow frequency drifts and we can solve this problem by adjusting ϕ_f (feedback loop phase or length) using a PZT. A small variation of ϕ_f changes f by

$$\eta_l = \frac{\partial f}{\partial \phi_f} = -\frac{1}{2\pi}\left[\frac{\partial \omega_\mathrm{N}}{\partial \omega}\right]^{-1}\frac{\partial \omega_\mathrm{N}}{\partial \phi_f}. \tag{2.3.20}$$

[4]It is easy to show (or infer from figure 2.3) that η is not very sensitive to $\phi_f + \theta$.

When $\phi_f + \theta = 0$ and $\omega_c \tau_c = 2\pi N$, we get [5]

$$\eta_l = -\frac{1-R}{2\pi}\mathrm{FSR_x} = -\mathrm{FWHM_x}/2. \tag{2.3.21}$$

For our experiment, η_l is -50 kHz/rad (or -0.46 kHz/nm in optical feedback loop length for the 689 nm laser). We control the feedback path length by using a PDH scheme, so that the laser frequency is locked tightly to the center of a cavity resonance.

To sum up, a small fraction of light coming from a laser diode is filtered by an external cavity and fed back to the diode for linewidth reduction. A PDH scheme controlling the optical feedback loop length is used to lock the laser to the center of a cavity resonance. By increasing the feedback level γ, laser linewidth can be reduced by a factor up to the finesse of the external cavity. The locking range is proportional to feedback level γ, but should be smaller than the FSR of the external cavity to avoid mode hopping. For an external cavity with a FSR of 1.5 GHz, the maximum γ is less than 0.01 [6] for a laser diode without AR coating.

[5] This gives the minimum η_l.

[6] Taking light loss and mode mismatching into consideration, we use about 2 percents of light power from the laser for optical feedback locking.

Chapter 3

Experimental Setup of a Narrow-Line Laser at 689 nm

Our setup has two essential parts: an optical feedback loop and a PDH setup that is controlling the phase of optical feedback. Two key issues of this setup are the design of a stable high-finesse cavity and mode matching between the external cavity and the diode laser.

3.1 Locking the Laser to the Cavity

Our high-finesse cavity has a FSR of 1.5 GHz and a finesse about 16000. The cavity has a small thermal expansion coefficient and its length can be tuned by Piezoelectric Transducers (PZT) at one end of it. The cavity is located in a vacuum chamber to isolate it from thermal and acoustic fluctuations.

3.1.1 The Cavity Design

The design of our cavity is illustrated in figure 3.1. Two identical concave mirrors, each with a radius of 25 cm and a reflectivity of 99.98% at 689 nm, form the cavity. One of these mirrors is glued directly by vacuum epoxy to one end of a Zerodur spacer, which has a nearly zero thermal expansion, while the second mirror is glued to a Macor ceramic ring and connected to the spacer by a pair of PZT tubes (with identical length for thermal expansion compensation) and a larger Macor ring. The larger Macor ring has a slit leaving space for wires connected to the PZTs. A small hole is drilled in the middle of the Zerodur spacer for air evacuation during vacuum pumping.

In our final set up, however, a mirror is glued on the inner side of the smaller Macor ring [1], so the cavity length becomes more sensitive to temperature. This allows us to tune the cavity length to the desired atomic transition by changing temperature.

[1]See figure A.5. More details of this cavity can be found in Appendix A.4.

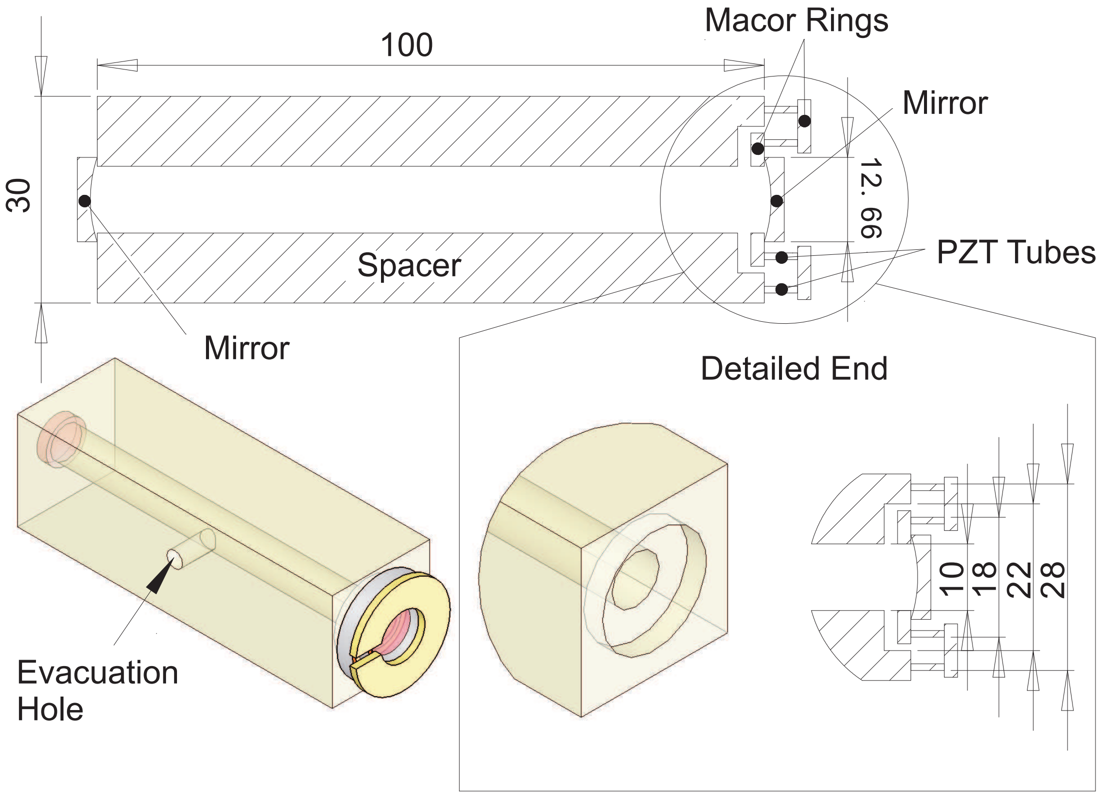

Figure 3.1: Design of the high-finesse cavity. Dimensions in mm.

To mechanically isolate the cavity, the spacer is held in a rectangular stainless steel block (figure 3.2), which is then located in a vacuum chamber (figure 3.3). The axis of the cavity is at an angle of 4° with respect to that of the steel block to avoid round-trip reflection between the mirrors of the cavity and windows of the vacuum chamber. Four outer edges of the steel block and middle lines of the inner rectangular hole are cut and filled with Viton rods [2]. The Zerodur spacer, the steel block and the chamber are tightly fixed by the rods. Wires of the PZT tubes are connected to a four channel feed-through. The chamber is pumped to 10^{-6} mbar and sealed.

To provide temperature control, a layer of electrical-insulating but thermal-conducting foil is used to cover the body of the vacuum chamber. Above it, thin heating wire is wound around at a spacing of 4 mm, giving a total resistance of 6 Ω. One 10 kΩ Negative Temperature Coefficient resistor (NTC) is attached to the vacuum chamber to monitor its temperature and facilitate temperature stabilization with a PID controller controlling the heating current. Finally, we cover the whole chamber with thermal insulating foam, leaving only two holes for light.

Speaking from our experience, we suggest, first, buying a spare set of Macor rings and PZT tubes since they are very fragile and may be destroyed during assembling or soldering. Second, soft wires should be soldered to the PZT tubes but connected

[2] Sections of Viton O-ring

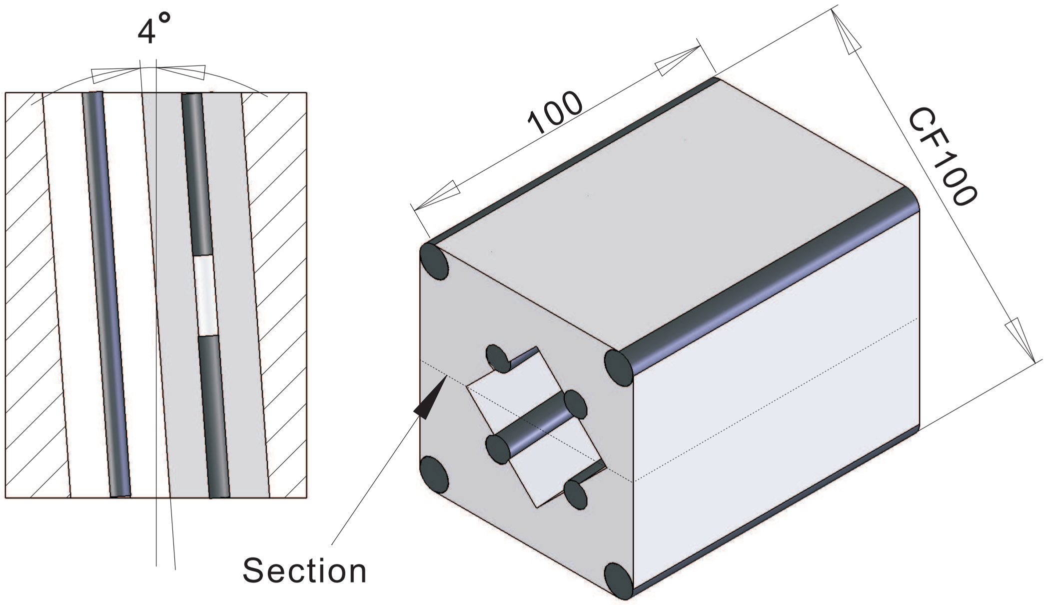

Figure 3.2: The steel block with Viton rods. Its diagonal matches the inner diameter of a CF100 tube. Its section at half-height is shown in the left panel. The axis of the cavity is at an angle of 4° with respect to that of the steel block. Dimensions in mm.

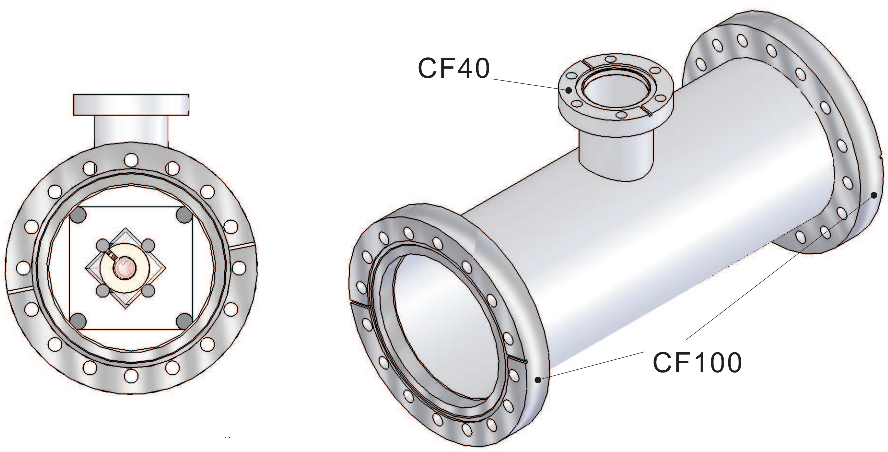

Figure 3.3: The vacuum chamber with the cavity inside it. This chamber is made from a 28 cm CF100 tube with one CF100 flange on each end for optical windows. A CF40 flange in the middle of the chamber is connected to a T connector, which has a valve and a four-pin feed-through on it.

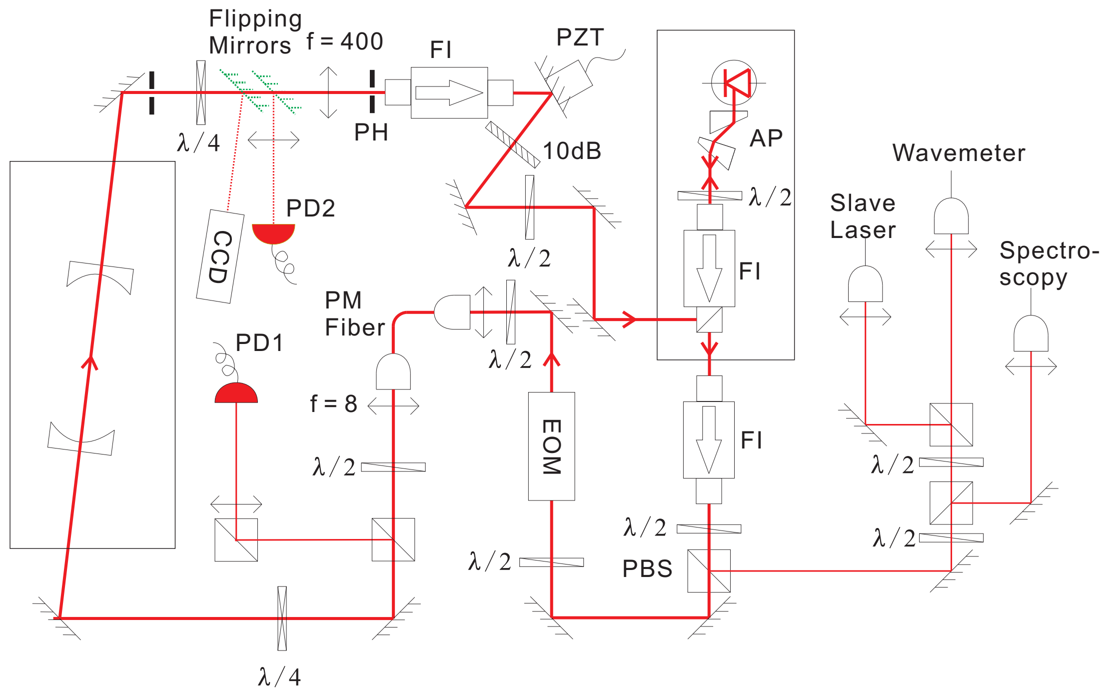

Figure 3.4: Schematic setup of our diode laser system with optical feedback from a high-finesse cavity. The thick red line shows the optical feedback path and the thin red line refers to the beams sent to other places. FI: Faraday isolator; EOM: Electro-Optic-Modulator; CCD: CCD camera without lens; PD: photo detector; 10dB: 10 dB attenuator; PH: pin hole; AP: anamorphic prism pair. Focus lengths in mm.

to feed-through pins via blade connectors because it is hard to heat up the thick pins. Third, when evacuating the chamber, the pumping speed should not be too high at the beginning. Otherwise air inside the cavity may have not time to evacuate and the cavity may 'explode'. We also make sure that the evacuation hole on the Zerodur spacer is not blocked by a Viton rod.

3.1.2 Alignment of the Optical Feedback

The guiding rule for our alignment is to achieve a good mode matching and a stable feedback loop. For this reason, the diode laser and the external cavity are both placed on a 60 cm × 90 cm stainless steel optical bread board, which rests itself above a layer of thick foam for acoustic isolation. Moreover, a compact alignment is helpful to reduce drift of alignment.

The schematic setup of our laser system is shown in figures 3.4. After a pair of anamorphic prisms and a half-wave plate, the light passes two 30 dB Faraday isolators in series. The reflected light (leakage) from the second PBS of the first isolator is adjusted to horizontal to facilitate alignment of optical feedback. An Electro-Optic

Modulator (EOM) is used to modulate the phase of the light at 38 MHz [3].

Afterwards, the light is coupled into a polarization maintaining single mode fiber for mode cleaning. A half-wave plate before the fiber coupler is used to match the polarization of the light with the optical axis of the fiber. After the fiber, the light power going to the cavity is maximized by a half wave plate and a PBS. An aspheric lens (f = 8 mm) in the fiber coupler is used to adjust the waist of the laser beam to match that of the cavity. Details of waist adjusting is discussed in Appendix A.2.

Once we achieve the right beam waist, two coupling mirrors before the cavity are used to match the waist location of the light with that of the cavity mode. The reflection from the cavity is detected by a fast (bandwidth $\approx$ 125 MHz) photo detector (PD1 in figure 3.4). Two flipping mirrors are placed after the cavity to reflect transmitted light to either a CCD camera (without the lens) or a slow photo detector. For alignment, we first overlap the reflection from the cavity to the incoming light. We then adjust the coupling mirrors and scan the length of the cavity to find a gaussian resonance using the CCD camera. After that, we maximize the transmission peak and reflection dip using the photo-detectors.

After coupling light into the cavity, the transmission is mode matched by a lens (f = 400 mm) and fed back to the laser diode. A 10 dB attenuator and a half wave plate are used to control the power of the feedback light. The feedback loop length is controlled by a small mirror driven by a PZT [4]. The leaked light from the second PBS of the first isolator is used as a reference in mode matching: the leaked light and the feedback light should overlap [5]. On the other hand, unwanted optical feedback caused by the leaked light should be eliminated. We do this by using a 30 dB Faraday isolator.

To complete the feedback, we first block the feedback path and tune the cavity resonance to the frequency of free running laser by monitoring the CCD. When we unblock the feedback path, the optical feedback can already force the diode to lase close to the cavity resonance. The reflection from the cavity is reduced by about 30% from the value without feedback. When this happens, the laser linewidth has been reduced by optical feedback, and the next task is to compensate frequency drift by controlling the feedback loop length.

To control the loop phase adjusting mirror, a PDH scheme is used (figure 3.4, electronics is shown in figure 3.5). Signal from the fast PD (PD1) is demodulated, processed by a PID controller [6] and converted to a high voltage output (with a range of 100 V) to drive a PZT holding the phase adjusting mirror.

In our setup, the output power of the laser diode is 15 mW and the light power

[3]The EOM is isolated by a piece of plastic from the supporting post to reduce radio frequency (RF) noise coupling to the optical table. A half-wave plate before the EOM optimizes phase modulation (PM) efficiency by matching the polarization of the light with the a certain axis of the EOM crystal. The light should pass the center of the EOM crystal and not be blocked by the shielding box to avoid interference nd amplitude modulation.

[4]See Appendix A.3 about how to make one.

[5]Two pinholes are used to mark the optical path of the transmission for ease of alignment.

[6]We use only a integrator with a bandwidth of 2 kHz.

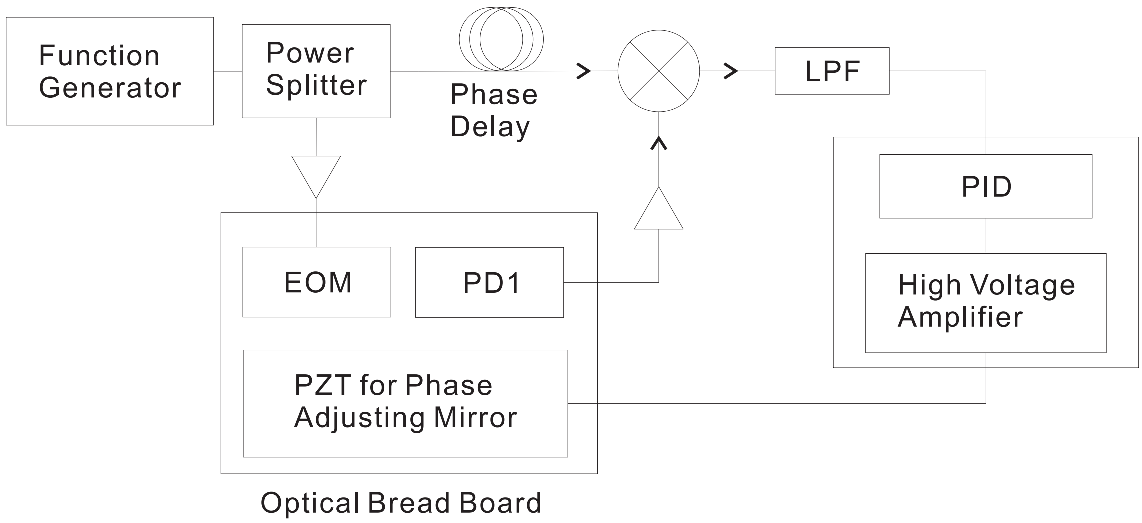

Figure 3.5: The electronics for optical feedback locking. PDH technique is used to tune the optical feedback phase. To maximize the amplitude of open-loop error signal (with optical feedback but no electrical feedback), the phase of the demodulation signal at mixer input is adjusted by changing cable length. LPF: Low pass filter.

before the cavity is about 250 μW. The feedback power measured before the PBS of the first isolator in figure 3.4 is about 5 μW corresponding to a feedback level γ of 0.02 [7]. The capture range is a few hundred MHz. When the optical feedback is working, the open loop (optical feedback length not controlled) dispersive PDH error signal has a peak-to-peak value about 200 mV while the close loop error signal has a RMS amplitude about 2 mV.

3.1.3 Linewidth Estimation of the Locked Laser

The standard way to estimate the linewidth of a laser is to beat it with another laser which has a similar frequency and a similar or narrower linewidth. Since we have only one 689 nm laser, we estimate its linewidth from the residual error signal when it is locked. Details of this technique are nicely discussed in reference [22] and [29], and their results are used here. When the modulation frequency is much larger than the linewidth of the cavity, the slope at the center of a PDH error signal is

$$D = 2V_{\mathrm{pp}}/\delta f,$$

where V_{pp} is the peak to peak amplitude of the dispersive PDH error signal; δf is the FWHM of the cavity resonance. In our experiment, we have D = 3.98 mV/kHz. Assuming a gaussian noise, the laser linewidth can be estimated via:

$$\mathrm{FWHM} = 2.355V_{\mathrm{rms}}/D.$$

[7] The real feedback level maybe lower than the measured one because of imperfect mode matching.

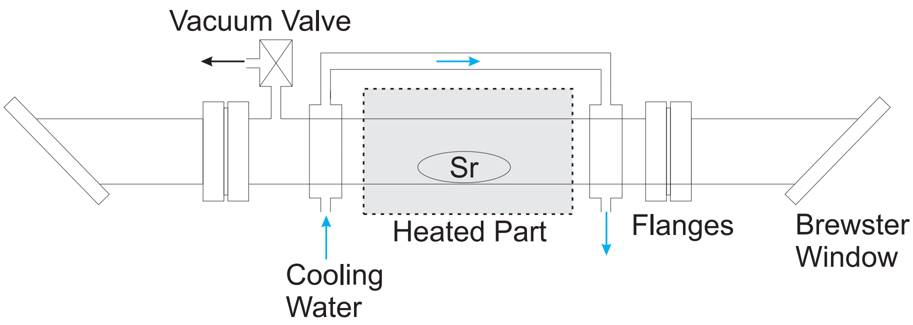

Figure 3.6: Schematic illustration of the Sr gas cell. Metallic strontium sample is located in the center of the heating pipe.

Since part of the error signal comes from background noises of electronics, we use

$$V_{\text{rms}}^2 = V_{\text{observed-rms}}^2 - V_{\text{background-rms}}^2$$

to get the RMS amplitude of the actual error signal . Taking the values that $V_{\text{observed-rms}} = 2.0$ mV and $V_{\text{background-rms}} = 0.7$ mV, we get FWHM = 1.1 kHz.

3.2 Locking the Cavity to the 689 nm Sr $^1S_0 -^3 P_1$ Transition

In section 3.1, we show a diode laser locked to a high-finesse cavity with a linewidth of about 1.1 kHz. To obtain a red MOT of strontium, the cavity resonance should be locked to the Sr $5s^2\ ^1S_0 - 5s5p^3P_1$ transition. Doppler-free saturation spectroscopy is used for this purpose. For an introduction to this technique, we suggest chapter 30 of Siegman's textbook 'LASERS' [18]. The design and performance of our spectroscopy system will be presented in this section. The key issue of our setup is to reduce the offset of the error signal caused by residual amplitude modulation.

3.2.1 The Strontium Gas Cell

Our strontium gas cell follows the design of [30] (figure 3.6). The heating pipe is made up of a stainless steel tube which has a diameter of 2.5 cm and a length of 60 cm. Its center part is wound with heating wires, glass fiber and aluminium foils to maintain a temperature near 530°C, at which the strontium vapor pressure is 1.46 Pa [31]. Each end of the heating pipe is water cooled and connected to another short pipe, which is terminated by a glass window at Brewster's angle. A small vacuum valve is connected to the heating pipe near one of its ends, and argon gas is filled in from the valve to act as a buffer gas preventing strontium coating on glass windows.

To feed metallic strontium into the center of the heating pipe, we operate in a transparent plastic bag filled with argon gas. To fill in the buffer gas, we repeatedly pump the gas cell (down to 10^{-3} mbar) and fill in argon (to higher than 1 bar) three times to eliminate residual air in the pipe. In the last time, we pump and fill in argon simultaneously. A flow-control valve is adjusted to achieve a pressure equilibrium at 10^{-2} mbar, then we close the valves.

3.2.2 Saturation Spectroscopy Setup

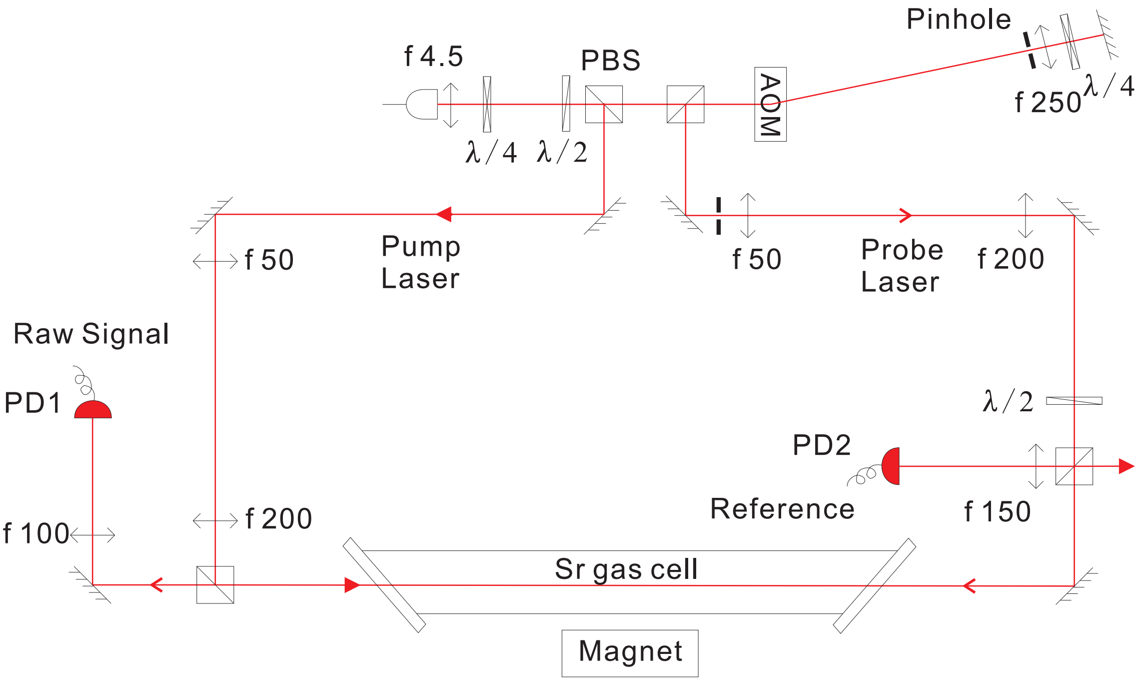

Figure 3.7: Saturation spectroscopy setup for locking the external reference cavity to Sr $^1S_0 -^3 P_1$ transition near 434.830 THz. f x refers to a lens with a focus length of x mm.

The saturation spectroscopy setup is shown in figure 3.7. Light from the diode locked to the external cavity is split into a pump beam (about 5 mW) and a probe beam (about 800 μW). A double-pass AOM shifts the probe frequency by +160 MHz to avoid interferences between the pump and the probe. Due to Doppler shift, the frequencies of pump and probe are only identical for a certain velocity group of atoms moving along the direction of probe light. Our spectroscopy setup thus lock the laser to a frequency 80 MHz above the unshifted atomic transition. The probe light is also frequency modulated (FM) by the AOM at a frequency of 124 kHz [8] to generate error signals of the spectroscopy.

Two telescopes are used to enlarge both the pump and the probe to a 5 mm waist before the gas cell. About half of the probe light is split and detected (PD2 in

[8]The RF frequency at the AOM is f = 80MHz+100kHz$\times$ sin($2\pi\times$124kHz$\times$t).

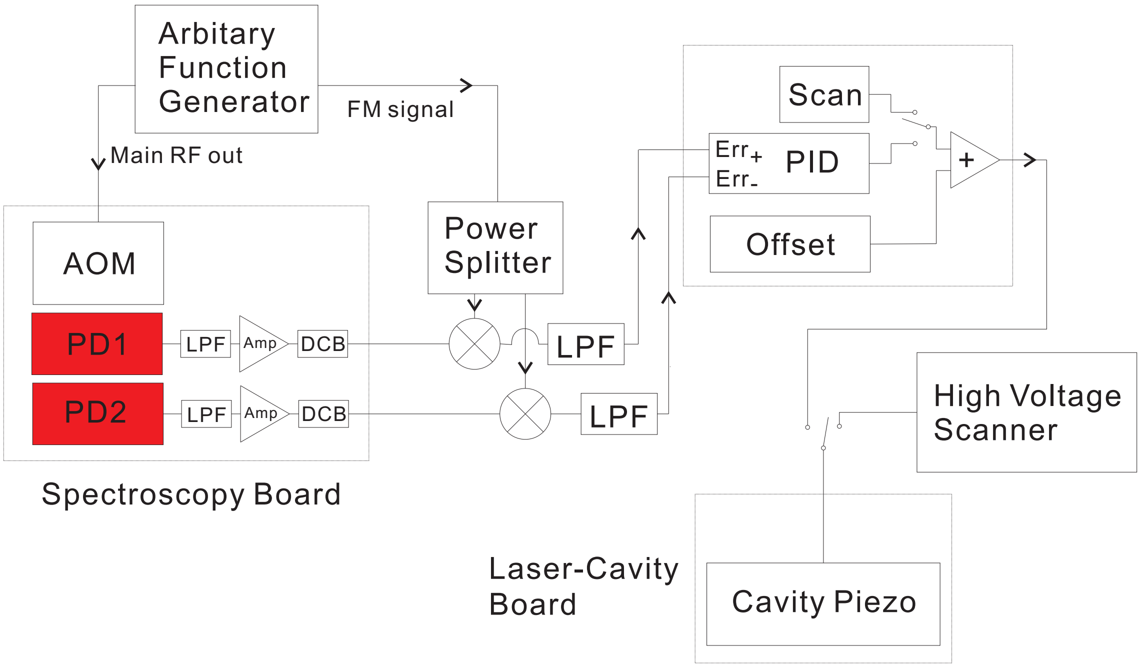

Figure 3.8: Electronic diagram of the spectroscopy setup for locking the laser to Sr $^1S_0 - ^3P_1$ transition near 434.830 THz. LPF: Low pass filter; DCB: DC block; frequency of the Main RF out: f = 80MHz+100kHz$\times$ sin($2\pi\times$124kHz$\times$t); FM signal has a frequency of 124 kHz.

figure 3.7) right before the strontium gas cell to monitor amplitude modulation of the probe. The other half of the probe passes through the gas cell and is detected (PD1 in figure 3.7) to generate an error signal after demodulation. A small magnet [9] is placed near the pipe center to increase splitting between different Zeeman sub-levels in the $^3P_1$ state. By scanning the light frequency near the atomic transition, we find a Doppler broadened absorption with a depth of 16% and a saturation peak with a height of 0.5%. The error signal corresponding to the center saturation peak ($m_J = 0$) is found to be about 800 kHz wide (i.e. frequency difference between the maximum and the minimum of the dispersive error signal) and 80 $\mathrm{mV_{pp}}$ high. This error signal has a drifting offset around 28 mV.

This offset of error signal is canceled by subtracting the error signal (demodulated from PD1) by the offset reference (demodulated from PD2). In our setup, identical electronics (figure 3.8) are used to process signals from PD1 and PD2. We can tune the light intensity ratio between PD1 and PD2 to match precisely the offset of the error signal with that of the reference [10]. These two signals are finally sent to the differential inputs of a PID controller driving the PZT of the cavity.

Regarding the electronics of the spectroscopy system (figure 3.8), since the FM frequency is about 124 kHz and the main frequency driving the AOM is at 80 MHz, the signals from photo-detectors are first filtered by 22.4 MHz low pass filters to eliminate noises at 80 MHz. Then a pair of first order RC DC-blocks transfer only AC signals to mixers. Demodulated signals from the mixers are filtered by 2nd order RC low pass filters and sent to the differential inputs of a PID controller. The whole servo loop of spectroscopy has a bandwidth about 10 Hz. We choose a FM frequency of 124 kHz simply for convenience since this is the lower frequency limit for usual commercial RF mixers. Our spectroscopy works properly at this FM frequency, but 124 kHz could still be too high for the AOM since the sound wave inside the crystal may vary too fast to have a homogeneous effect on the laser beam. Amplitude modulation could happen due to this and may be the main drawback in our setup. To improve this system, we want to decrease the FM frequency to about 10 kHz by replacing the mixer by a lock-in amplifier in the future [11].

3.2.3 Locking Procedure of the Laser

Since the saturation spectroscopy spectrum is broad and strong enough to be observed by using free-running laser, we first block the optical feedback path and tune the diode driving current to the atomic transition [12] by observing the saturation absorption

[9] We use a magnet from a small loud-speaker.

[10] In our experiment, the powers before PD1 and PD2 are 466μW and 346μW respectively. This difference comes mainly from the none-identical behaviors of electronics. However, we can also take advantage of this phenomena - we tune the FM frequency a bit (about 30 kHz in 124 kHz), then the offsets in these two channels will response differently and be matched.

[11] See the Appendix for details.

[12] The frequency difference between the free-running laser and the atomic transition should be smaller than the capture range of the cavity.

peak. After that, we tune a cavity resonance to the frequency of the free-running laser by adjusting the voltage on the cavity PZT. Then, we unblock the feedback path to lock the diode laser to the cavity and scan the cavity near the atomic transition to observe a clean saturation peak and a dispersive error signal.

By adjusting the temperature of the cavity, we ensure that the external cavity is resonant to the $^1S_0 -^3 P_1$ transition while the voltage applied on the cavity PZT is within the output range (± 12 V) of a low noise PID controller. By turning off cavity scan and turning on the PID controller, the laser is locked to the atomic transition.

3.2.4 Performance of the Red Laser

Similar to the analysis in locking the diode laser to the cavity, when the FM frequency is much smaller than the linewidth of the atomic transition, and assuming a Lorentz shape line profile, the slope in the center of the error signal is

$$D = 3.08 V_{\mathrm{pp}}/\delta f,$$

where V_{pp} is the peak to peak amplitude of open-loop dispersive error signal and δf is the FWHM of the broadened atomic transition. From the RMS amplitude of the close-loop error signal, we get a frequency uncertainty about 10 kHz.

For a strontium red MOT experiment, the linewidth of the 689 nm laser limits the minimum atomic temperature achievable. The small drift of the laser frequency (caused mainly by residual amplitude modulation) moves the MOT position a bit but is not harmful to the final result. With this red laser, our group has got the red MOT of strontium with an atom number of 2×10^7 and an atom temperature of 2.5 μK, which is consistent with our estimation from the laser linewidth. A picture of this MOT is shown in figure 3.9.

3.3 Conclusions

To conclude, by using optical feedback from a high-finesse cavity, the linewidth of a laser diode is reduced to about 1 kHz. Frequency drift of this laser is compensated by locking the laser to the Sr $^1S_0 -^3 P_1$ transition with an uncertainty of 10 kHz. This laser system is easy to set up (about one week) and not demanding in electronics. The bandwidths of the electrical servo systems used in optical feedback and spectroscopy are only 2 kHz and 10 Hz respectively. There are also rooms for the system to be improved. First, due to temperature and current drifts, the laser frequency may drift out of the locking range in roughly every 30 minutes. A better temperature PID can solve this problem. Second, we have to try several laser diodes to find a ‘good’ one that can lase stably at the desired atomic transition. Some work may be done to find a certain brand or batch of diodes that are suitable for this setup. This laser system is suggested to be a feasible quick solution for strontium laser cooling applications.

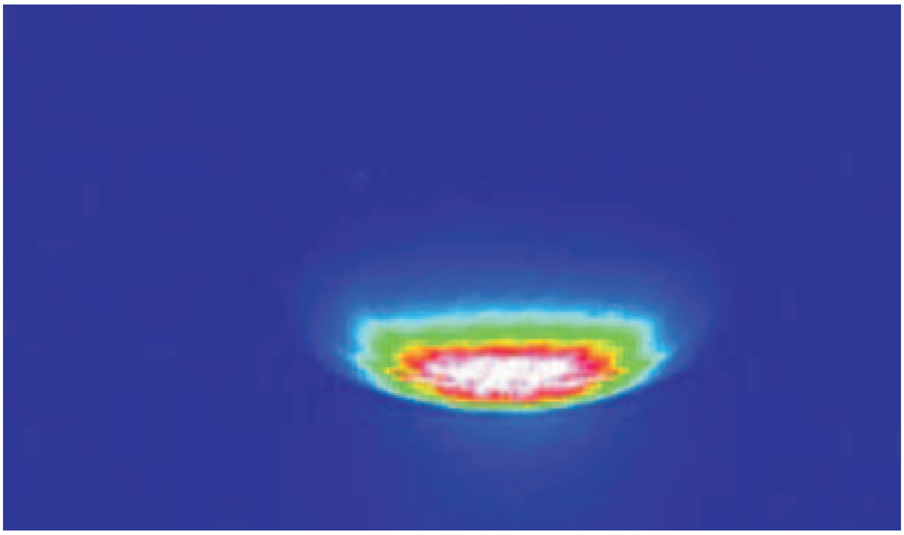

Figure 3.9: Absorption image of a strontium red MOT along the horizontal direction. Sr $^1S_0$-$^3P_1$ transition's natural width is similar to its recoil frequency shift, so atoms can interact with the MOT laser only in a thin elliptical shell where laser frequency shift compensates Zeeman shift. The maximum radiation force is only one order of magnitude larger than the gravity force, so atoms rest on the bottom of the shell.

Chapter 4

Publication: Bose-Einstein Condensation of Strontium

† Physical Review Letters **103**, 200401 (2009)

Simon Stellmer[1,2], Meng Khoon Tey[1], Bo Huang[1,2], Rudolf Grimm[1,2] and Florian Schreck[1]

[1] *Institut für Quantenoptik und Quanteninformation (IQOQI), Österreichische Akademie der Wissenschaften, 6020 Innsbruck, Austria*

[2] *Institut für Experimentalphysik und Zentrum für Quantenphysik, Universität Innsbruck, 6020 Innsbruck, Austria*

We report on the attainment of Bose-Einstein condensation with ultracold strontium atoms. We use the ^{84}Sr isotope, which has a low natural abundance but offers excellent scattering properties for evaporative cooling. Accumulation in a metastable state using a magnetic trap, narrow-line cooling, and straightforward evaporative cooling in an optical trap lead to pure condensates containing 1.5×10^5 atoms. This puts ^{84}Sr in a prime position for future experiments on quantum-degenerate gases involving atomic two-electron systems.

Ultracold gases of strontium atoms have been attracting great attention for various reasons. A major driving force for the development of cooling and trapping techniques since the early 1990s [32] has been the realization of ultraprecise optical clocks [33, 34, 35]. Many other intriguing applications related to metrology [9], novel schemes for quantum computation [3, 4], and quantum simulators of unique many-body phenomena [5, 36] rely on the special properties of this species. Moreover, there is considerable interest in ultracold Sr_2 molecules [7, 37] and their possible applications for testing the time variation of fundamental constants [38]. Ultracold plasmas

†The primary contribution of the author of the present thesis is the setup of the narrow-line master laser as described in chapters 2 and 3 of this thesis.

[39] represent another fascinating application of strontium atoms. Many of the possible experiments could greatly benefit from the availability of quantum-degenerate samples.

The two valence electrons of strontium and the resulting singlet and triplet states are at the heart of many of these applications. The two-electron nature also has very important consequences for cooling and trapping strategies towards degeneracy. Because of its singlet character the electronic ground state does not carry a magnetic moment. Therefore optical dipole traps [40] are the only option to implement evaporative cooling. Moreover, magnetic Feshbach resonances, frequently applied to tune the scattering properties of other atomic systems [41], are absent. Research on Bose-Einstein condensation (BEC) and degenerate Fermi gases involving atomic two-electron systems was pioneered by the Kyoto group, using various isotopes of Yb [11, 42, 43, 44]. Very recently, a BEC of ^{40}Ca was produced at the Physikalish-Technishe Bundesanstalt in Braunschweig [10].

Experiments towards quantum degeneracy in strontium have so far been focussed on the three relatively abundant isotopes ^{86}Sr (9.9%), ^{87}Sr (7.0%), ^{88}Sr (82.6%), the first and the last one being bosons. The necessary phase-space density for BEC or Fermi degeneracy could not be achieved in spite of considerable efforts [45, 46]. For the two bosonic isotopes the scattering properties turned out to be unfavorable for evaporative cooling [46]. The scattering length of ^{88}Sr is close to zero, so that elastic collisions are almost absent. In contrast, the scattering length of ^{86}Sr is very large, leading to detrimental three-body recombination losses. As a possible way out of this dilemma, the application of optical Feshbach resonances [41] to tune the scattering length is currently under investigation [47, 48].

In this Letter, we report on the attainment of BEC in ^{84}Sr. This isotope has a natural abundance of only 0.56% and, apparently for this reason, has received little attention so far. We show that the low abundance does not represent a serious disadvantage for BEC experiments, as it can be overcome by an efficient loading scheme. Because of the favorable scattering length of $+123\,a_0$ (Bohr radius $a_0 \approx 53\,\mathrm{pm}$) [49, 50, 51] there is no need of Feshbach tuning, and we can easily produce BECs containing 1.5×10^5 atoms.

Our experimental procedure can be divided into three main stages. In the first stage, the atoms are accumulated in a magnetic trap, using a continuous loading scheme based on optical pumping into a metastable state. In the second stage, the atoms are first pumped back into the electronic ground state, laser cooled using a narrow intercombination line, and loaded into an optical dipole trap (ODT). In the third stage, evaporative cooling is performed by lowering the depth of the ODT and, thanks to the excellent starting conditions and collision properties, BEC is attained in a straightforward way.

The accumulation stage takes advantage of magnetically trapped atoms in the metastable triplet state $^3P_2$; see Fig. 4.1. Remarkably, such atoms are automatically produced [45, 46, 52, 53, 54, 55, 56] when a standard magneto-optical trap (MOT)

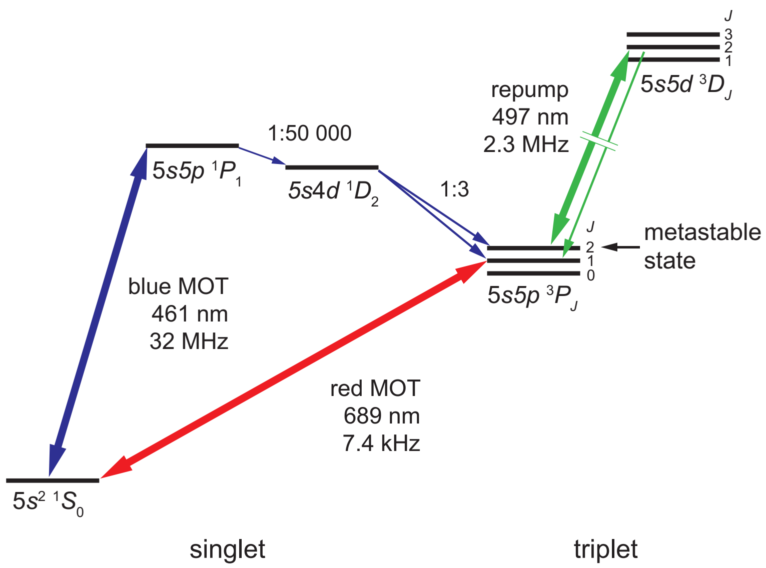

Figure 4.1: Schematic illustration of the energy levels and transitions used for cooling and trapping of strontium atoms. The blue MOT is operated on the strong $^1S_0$-$^1P_1$ transition. The loading of the magnetic trap proceeds via the weak leak of the excited state (branching ratio 1:50 000) into the $^1D_2$ state, which itself decays with a 1:3 probability into the metastable $^3P_2$ state. Here the atoms can be magnetically trapped and accumulated for a long time. The transition $^3P_2$-$^3D_2$ allows to depopulate the metastable state by transfering the atoms into the $^3P_1$ state. The latter represents the excited state of the $^1S_0$-$^3P_1$ intercombination line, used for narrow-line cooling in the red MOT.

is operated on the strong $^1S_0$-$^1P_1$ transition at a wavelength of 461 nm [1]. A weak leak of the excited state out of the cooling cycle of this "blue MOT" continuously populates the metastable state and the atoms are trapped in the magnetic quadrupole field of the MOT. This continuous magnetic-trap loading mechanism is our essential tool to prepare a sufficiently large number of ^{84}Sr atoms despite of the low natural abundance of this isotope. With a steady-state number of about 3×10^5 atoms in the blue MOT, we can reach an estimated number of roughly 10^8 atoms in the magnetic trap after typically 10 s of loading. This enormous gain is facilitated by the long lifetime of about 35 s for the magnetically trapped atoms under our ultrahigh vacuum conditions, which is about three orders of magnitude larger than the leak time constant of the blue MOT. Note that the same scheme has been applied to increase the number of ^{84}Sr atoms for spectroscopic measurements [56]. Also note that a very similar loading scheme was crucial for the attainment of BEC in Cr [57].

In the narrow-line cooling stage, a MOT is operated on the $^1S_0$-$^3P_1$ intercombination line (wavelength 689 nm, linewidth 7.4 kHz) using a scheme pioneered by Katori *et al.* [58], which has become an almost standard tool for the preparation of ultracold Sr. Loading of this "red MOT" [2] is accomplished by pumping the atoms out of the metastable reservoir using a flash of laser light resonant with the $^3P_2$-$^3D_2$ transition at 497 nm [9]; see Fig. 4.1. In the initial transfer phase, the magnetic field gradient is reduced from 61 G/cm as used for the magnetic trap to 3.6 G/cm within about 0.1 ms. To increase the capture velocity of the red MOT we frequency-modulate the light, producing sidebands that cover a detuning range between -250 kHz and -6.5 MHz with a spacing of 35 kHz; here each of the MOT beams has a waist of 5 mm and a peak intensity of 10 mW/cm^2. In a compression phase, the red MOT is then slowly converted to single-frequency operation with a detuning of about -800 kHz by ramping down the frequency modulation within 300 ms. At the same time the intensity of the MOT beams is reduced to 90 μW/cm^2 and the magnetic field gradient is increased to 10.4 G/cm. At this point, we obtain 2.5×10^7 atoms at a temperature of 2.5 μK in an oblate cloud with diameters of 1.6 mm horizontally and 0.4 mm vertically.

To prepare the evaporative cooling stage, the atoms are transferred into a crossed-beam ODT, which is derived from a 16-W laser source operating at 1030 nm in a single longitudinal mode. Our trapping geometry follows the basic concept successfully applied in experiments on Yb and Ca BEC [10, 11, 42, 44]. The trap consists of

[1]Loading of the blue MOT follows standard laser cooling and trapping procedures. Atoms emitted from an effusive beam source are transversely laser cooled to increase the loading flux of the low-abundant isotope. They are the Zeeman slowed to be captured by the MOT. Our MOT laser beams have a waist of 9 mm, a peak intensity of 5 mW/cm^2, and a detuning of -33 MHz. The quadrupole magnetic field has a gradient of 61 G/cm along its symmetry axis. The temperature in the MOT is Doppler-limited to a few mK.

[2]The 689-nm laser system is a master-slave combination. The master laser is stabilized on a 100 kHz linewidth cavity by optical feedback, resulting in a linewidth of $\sim$2 kHz. The laser frequency is locked to the ^{88}Sr intercombination line and frequency shifted by 351.4 MHz to the red to account for the isotope shift. A 30-mW slave laser diode is injection locked to the master to obtain sufficient light for the MOT. The red light is superimposed with the blue MOT beam using dichroic mirrors.

a horizontal and a vertical [3] beam with waists of $32\,\mu$m and $80\,\mu$m, respectively. Initially the horizontal beam has a power of 3 W, which corresponds to a potential depth of $110\,\mu$K and oscillation frequencies of 1 kHz radially and a few Hz axially. The vertical beam has 6.6 W, which corresponds to a potential depth of $37\,\mu$K and a radial trap frequency of 250 Hz. Axially, the vertical beam does not provide any confinement against gravity. In the crossing region the resulting potential represents a nearly cylindrical trap [4]. In addition the horizontal beam provides an outer trapping region of much larger volume, which is of advantage for the trap loading.

The dipole trap is switched on at the beginning of the red MOT compression phase. After switching off the red MOT, we observe 2.5×10^6 atoms in the ODT with about 10^6 of them residing in the crossed region. At this point we measure a temperature of $\sim10\,\mu$K, which corresponds to roughly one tenth of the potential depth and thus points to plain evaporation in the transfer phase. We then apply forced evaporative cooling by exponentially reducing the power of both beams with a $1/e$ time constant of ~3 s [5]. The evaporation process starts under excellent conditions, with a peak number density of $1.2\times10^{14}\,\mathrm{cm}^{-3}$, a peak phase-space density of $\sim2\times10^{-2}$, and an elastic collision rate of about $3500\,\mathrm{s}^{-1}$. During the evaporation process the density stays roughly constant and the elastic collision rate decreases to $\sim700\,\mathrm{s}^{-1}$ before condensation. The evaporation efficiency is very large as we gain at least three orders of magnitude in phase-space density for a loss of atoms by a factor of ten.

The phase transition from a thermal cloud to BEC becomes evident in the appearance of a textbook-like bimodal distribution, as clearly visible in time-of-flight absorption images and the corresponding linear density profiles shown in Fig. 4.2. At higher temperatures the distribution is thermal, exhibiting a Gaussian shape. Cooling below the critical temperature T_c leads to the appearance of an additional, narrower and denser, elliptically shaped component, representing the BEC. The phase-transition occurs after 6.3 s of forced evaporation, when the power of the horizontal beam is 190 mW and the one of the vertical beam is 410 mW. At this point, with the effect of gravitational sag taken into account, the trap depth is 2.8μK. The oscillation frequencies are 59 Hz in the horizontal axial direction, 260 Hz in the horizontal radial direction, and 245 Hz in the vertical direction.

For the critical temperature we obtain $T_c = 420\,\mathrm{nK}$ by analyzing profiles as displayed in Fig. 4.2. This agrees within 20%, i.e. well within the experimental uncertainties, with a calculation of T_c based on the number of 3.8×10^5 atoms and the trap frequencies at the transition point. Further evaporation leads to an increase of the condensate fraction and we obtain a nearly pure BEC without discernable thermal fraction after a total ramp time of 8 s. The pure BEC that we can routinely produce

[3] For reasons of optical access the beam is not exactly vertical, but inclined by 20°.

[4] To avoid perturbations by interference effects the beams are orthogonally polarized and have a frequency difference of 160 MHz.

[5] The evaporation process turns out to be very robust, and common or individual variations of the ramping time constants for both beams are not found to have strong effects on the evaporation efficiency.

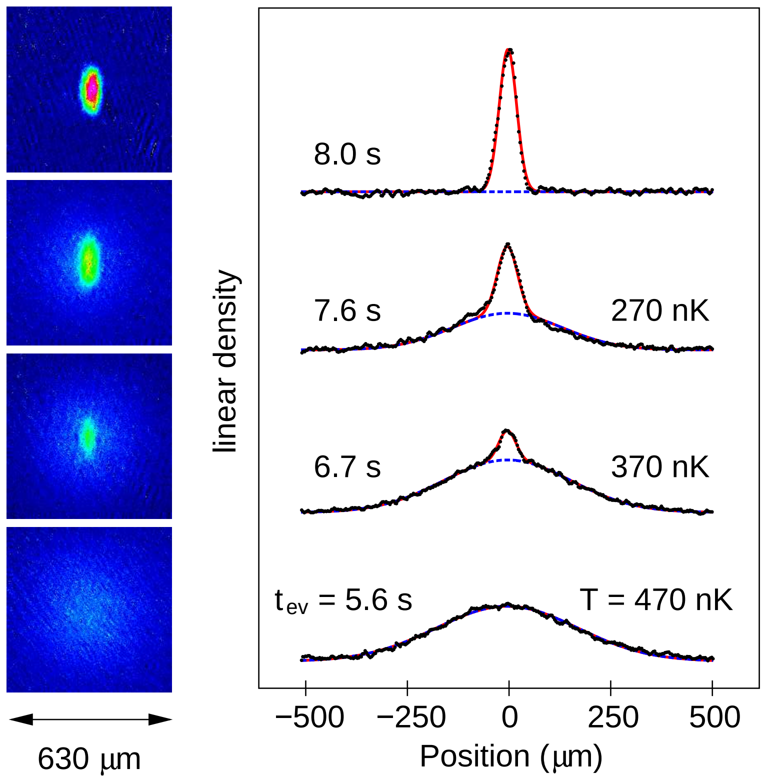

Figure 4.2: Absorption images and integrated density profiles showing the BEC phase transition for different times t_{ev} of the evaporative cooling ramp. The images are along the vertical direction 25 ms after release from the trap. The solid line represents a fit with a bimodal distribution, while the dashed line shows the Gaussian-shaped thermal part, from which the given temperature values are derived.

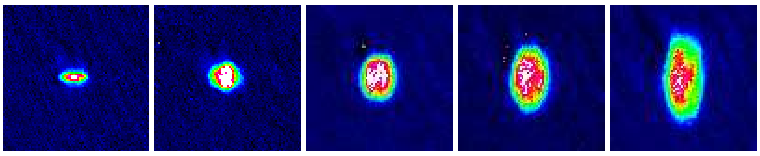

Figure 4.3: Inversion of the aspect ratio during the expansion of a pure BEC. The images (field of view 250μm $\times$ 250μm) are taken along the vertical direction. The first image is an in-situ image recorded at the time of release. The further images are taken 5 ms, 10 ms, 15 ms, and 20 ms after release.

in this way contains 1.5×10^5 atoms and its lifetime exceeds 10 s.

The expansion of the pure condensate after release from the trap clearly shows another hallmark of BEC. Fig. 4.3 demonstrates the well-known inversion of the aspect ratio [59, 60], which results from the hydrodynamic behavior of a BEC and the fact that the mean field energy is released predominantly in the more tightly confined directions. Our images show that the cloud changes from an initial prolate shape with an aspect ratio of at least 2.6 (limited by the resolution of the in-situ images) to an oblate shape with aspect ratio 0.5 after 20 ms of free expansion. From the observed expansion we determine a chemical potential of $\mu/k_B \approx 150\,\mathrm{nK}$ for the conditions of Fig. 4.3, where the trap was somewhat recompressed to the setting at which the phase transition occurs in the evaporation ramp. Within the experimental uncertainties, this agrees with the calculated value of $\mu/k_B \approx 180\,\mathrm{nK}$.

It is interesting to compare our number of 1.5×10^5 atoms in the pure BEC with other BECs achieved in two-electron systems. For ^{174}Yb up to 6×10^4 atoms were reported [44], and for ^{40}Ca the number is 2×10^4 [10]. It is amazing that our BEC clearly exceeds these values with little efforts to optimize the number after our first sighting of BEC (26 Sept. 2009). We anticipate that there is much more room for improvements in particular in the transfer from the red MOT into the ODT. We interpret the amazing performance of ^{84}Sr as the result of a lucky combination of favorable scattering properties with excellent conditions for narrow-line cooling, and we believe that this makes ^{84}Sr a prime candidate for future experiments on BEC with two-electron systems.

We finally discuss a few intriguing applications which seem to be realistic on a rather short time scale. The ^{84}Sr BEC may serve as an efficient cooling agent to bring other isotopes into degeneracy. A BEC of ^{88}Sr would be a non-interacting one [41], as the intra-isotope scattering length is extremely small [46, 51]. This would constitute a unique source of low-momentum, non-interacting, and magnetically insensitive atoms, ideal for precision measurements [9]. The fermionic isotope ^{87}Sr offers a nuclear spin decoupled from the electronic degrees of freedom, which is very favorable for quantum computation [3, 4] and the essential key to a new class of many-body physics with ultracold atoms [5, 36]. The realization of a Mott insulator state appears to be a straightforward task [61]. Another fascinating application would be the creation of ultracold dimers made of an alkali atom and a two-electron atom [62]. Since all-optical evaporative cooling strategies for ^{87}Rb and ^{84}Sr proceed under very similar conditions [63, 64, 65], the creation of SrRb molecules seems to be a realistic option. Such molecules would be qualitatively different from the bialkali atoms currently applied in heteronuclear molecule experiments [66] as they offer a magnetic rovibrational ground state [62].

We thank Andreas Trenkwalder and Christoph Kohstall for technical assistance with the dipole trap laser. We furthermore thank Andrew Daley, Peter Zoller, and Hanns-Christoph Nägerl for stimulating discussions on the prospects of strontium for future experiments. We also acknowledge fruitful discussions with Jun Ye, Thomas Killian, and Yoshiro Takahashi.

Appendix A

Experiment Details

A.1 Toptica DL Pro Laser

Before using optical feedback locking, we tried to reduce the laser linewidth by electrical feedback. The 689 nm grating stabilized laser we have is a 'DL pro' from Toptica. This laser allows us to modulate the diode current from DC to 50 MHz via a 50 Ω terminated BNC voltage input. To obtain light frequency response of the laser head to input voltage, we modulate the laser with sinusoidal signals at different frequencies and measure the transmission through a low finesse (less than 10) cavity. Since the laser is modulated at the edge of the transmission profile where transmission changes almost linearly with light frequency, the transmission variation tells us the frequency variation of the light. Comparing the measured light frequency variation with the input modulation signal, we get the FM sensitivity (in Hz/mV) and the FM phase delay of the laser head as functions of modulation frequency. The setup for this purpose is illustrated in figure A.1.

The result in the frequency range from 10 kHz to 10 MHz is shown in figure A.2. The overall trend of the response looks like a low-pass filter. However, the modulation sensitivity has a sharp drop at 60 kHz down to about 1/3 of the value expected from

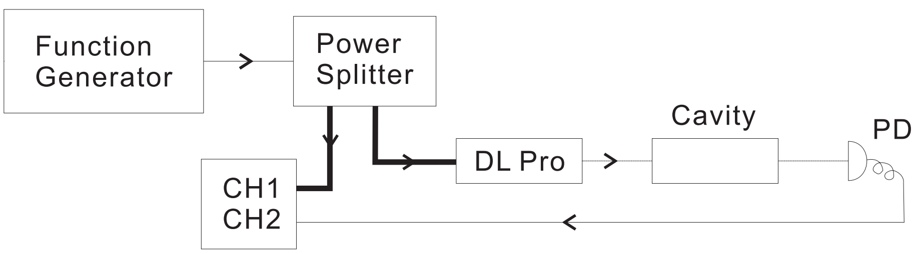

Figure A.1: The setup for testing light frequency response of the laser head to voltage input. Thick lines represent BNC cables with identical lengths. CH1 and CH2: Channel 1 and 2 of the oscilloscope; PD: fast photo-detector with a bandwidth of 125 MHz.

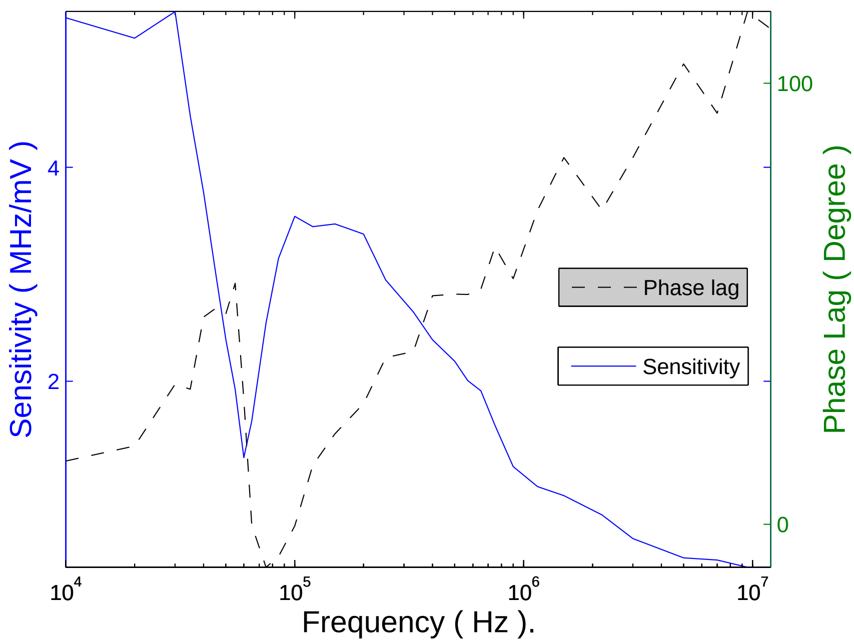

Figure A.2: Light frequency response of DL-Pro laser head to voltage input. The solid line is the laser's frequency modulation (FM) sensitivity to input voltage (in Hz/mV) and the dashed line is its FM phase lag.

the over all trend. A phase dispersion at the same frequency confirms this dip.

When we locked the laser to a cavity with 1 MHz linewidth by using PDH technique, a typical power spectrum of the error signal after locking is shown in figures A.3. The weak frequency response near 60 kHz leads to a residual noise peak about 10 dB higher than the background. Moreover, our DL-Pro laser at 689 nm has a measured linewidth around 400 kHz, which is much higher than the typical linewidth (100 kHz) of DL-Pro lasers at other wavelengths. If electrical feedback is used for linewidth reduction, such a noisy laser source is very demanding in servo electronics. We run away from this problem by using optical feedback, but we will be back in the future.

A.2 Light Mode Adjusting by a Single Lens

In our setup, only one lens at the fiber coupler is needed for mode matching into the reference cavity. This trick is illustrated in figure A.4. Since the light coming out from the fiber is highly diverged at an angle of θ, the beam radius ($1/e^2$ intensity) w right after the fiber coupler is determined by the focus length of the collimation lens by $w = f\sin(\theta/2)$. If we move the position of the lens slightly outward from the collimation position, the laser will be focused but the beam size at the coupler is almost unchanged. To match the beam waist with waist of the cavity mode, w_0, the

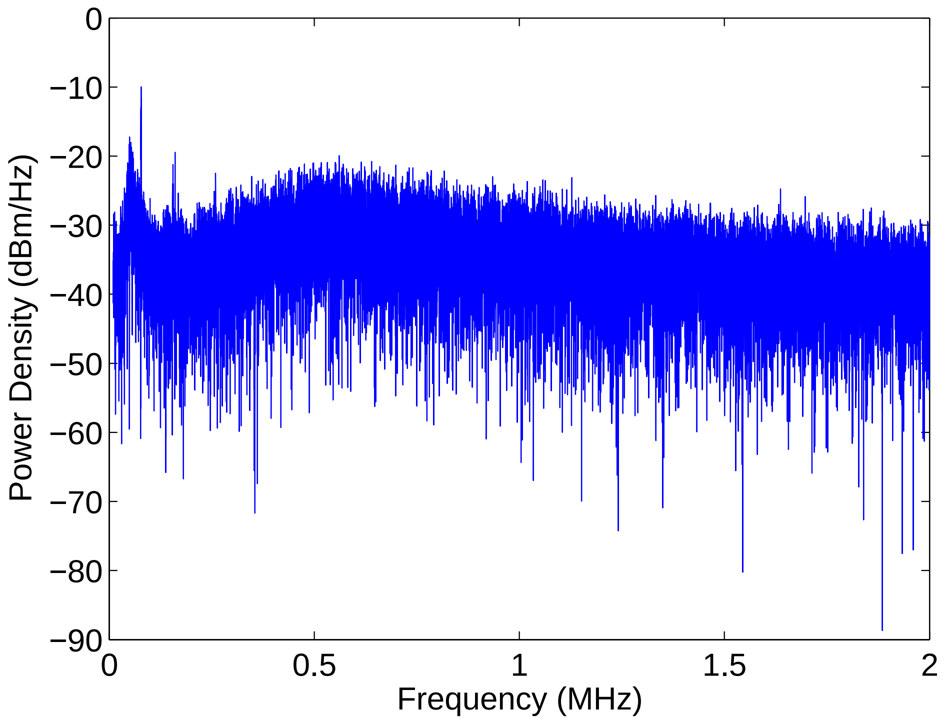

Figure A.3: Power spectrum of error signal when the DL-Pro laser is locked to a cavity with about 1 MHz linewidth by using electrical feedback. Parameters are optimized and the loop gain is maximized before the lock goes into oscillation. Weak sensitivity of the laser head at 60 kHz leads to a bump about 10 dB high there.

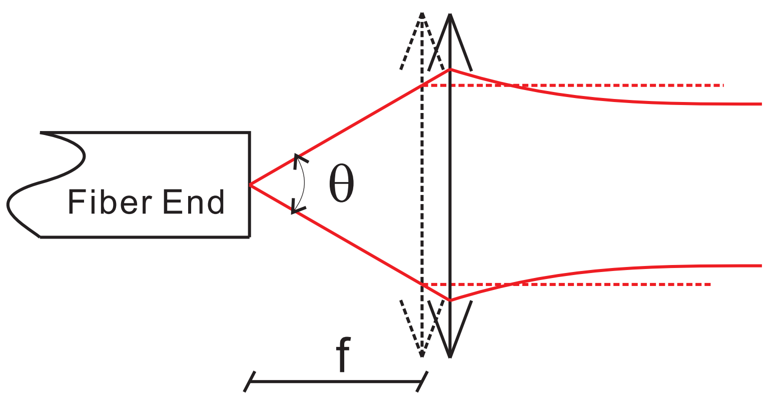

Figure A.4: The laser beam size is determined by the focus length of the lens at fiber coupler. After collimation, slightly moving the lens outwards can focus the laser while its beam size at the coupler is almost unchanged. The solid lines show a focused beam and corresponding lens position while the dashed lines show a collimated beam.

following equation should be satisfied:

$$z = z_R\sqrt{(\frac{w}{w_0})^2 - 1}, \tag{A.2.1}$$

Where z is the distance between collimation lens and beam waist, and $z_R = \pi w_0^2/\lambda$ is the Rayleigh length. In our experiment, a lens with $f = 8$ mm gives a convenience z of 56 cm. Due to extra optical length caused by the chamber window, PBS and the first mirror of the cavity as well as the concave lens effect from this mirror, the final distance between the cavity center and the collimation lens is about 2 cm shorter than the result from (A.2.1). Since z_R is about 10 cm in our experiment, a focus distance uncertainty less than 3 cm has no significant effect.

A.3 Phase Adjusting Mirror

To achieve a higher locking bandwidth, the phase adjusting mirror and PZT system (in figure 3.4) should have a high resonance frequency. A low mass mirror, a small and hard PZT tube and a heavy mounting block are helpful. In our setup, a mirror with dimensions of $5 \times 5 \times 1$ mm^3 is glued on a small PZT tube with dimensions of $3 \times 4 \times 5$ mm^3. This PZT is then glued to a cylinder aluminium block on a usual mirror mount. To cut the small mirror from a common one that is 1 inch in diameter, we use cosmetic nail polish to protect the mirror surface during machining and wash it away by acetone afterwards. Wax or removable glue can be used to fix the mirror during cutting.

A.4 Temperature Characteristics of the Reference Cavity

In the original design, the length of the cavity is tuned only by the voltages applied on its two PZT tubes. A high voltage battery set is used for one PZT for coarse tuning (175 V for one FSR) while the other PZT is driven by a PID controller with a small voltage output range. This cavity should be insensitive to temperature variation.

However, in our final setup, one mirror is glued inside rather than outside of the inner Macor ring (figure A.5). Consequently, the cavity length is reduced by the thickness of the mirror and that of the smaller ceramic ring. This difference leads to a larger FSR of 1.58 GHz and a much lager thermal expansion effect [1]. On one hand, this forces us to stabilize the temperature of the cavity more precisely. On the other, we can tune the cavity length by adjusting temperature (+157 MHz/K) instead of using a battery stack. Since temperature are relatively easy to be stabilized while batteries would age, coarse tuning of cavity length by temperature is more convenient.

[1]The expansion of Zerodur spacer is only 22.5% of that of the mirror and the ceramic ring.

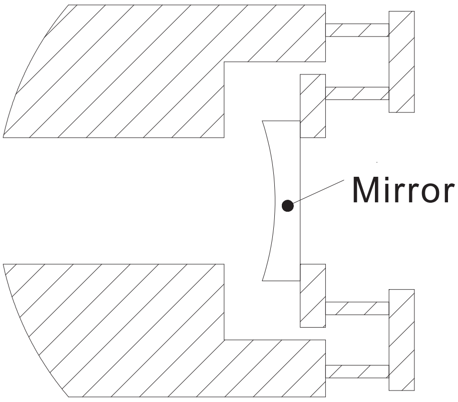

Figure A.5: The final setup of the cavity end with PZTs. The mirror is glued on the inner side of the small Marco ring instead of on the outer side. Due to the thickness of the mirror and that of the small Macor ring, the cavity length is reduced slightly and becomes more sensitive on temperature variation.

Every time after we change the temperature, one day is needed for thermal stabilization. Once the right temperature is obtained so that the cavity resonance is in the capture range of the spectroscopy PID controller (± 12 V), this system will work stably for weeks.

A.5 Analysis of the Sr Spectroscopy Signal

Although the Sr 689 nm transition only has a natural linewidth of 7.4 kHz, its doppler free saturation spectroscopy signal is greatly broadened due to collisions, power saturation, residual doppler effect and transition broadening. We estimate its broadened linewidth at 530 K in our system in the following discussion.

For collisions, data and equations can be found in [31] and [67]:

$$\begin{aligned}
\sigma_{SrSr} &= (6.55 \pm 0.6) \times 10^{-14}\ \mathrm{cm}^2 \\
\sigma_{SrAr} &= (1.52 \pm 0.18) \times 10^{-14}\ \mathrm{cm}^2 \\
\log P_{Sr} &= 9.584 \pm 0.132 - \frac{7566 \pm 101}{T} \\
N_i &= P_i/(k_B T) \\
\Delta f &= \frac{1}{\pi} \sum N_i \langle \sigma_i v_i \rangle.
\end{aligned}$$

σ_{SrSr} is the cross section between Sr atoms, σ_{SrAr} is that between Sr and Ar atoms. P_{Sr} is the vapor pressure of Sr in Pa. T is in a range from 673 K to 873 K. N_i and P_i are the density and pressure of the ith collision partner respectively, and σ_i the cross section and v_i the center-of-mass velocity of the two colliders. The collisional broadening for Sr 689 nm line is about 300 kHz and the mean-free-path is about 6 mm.

Transition broadening is calculated from

$$\Delta\omega = 1/\Delta t = \bar{v}/d,$$

where d is the diameter of the probe beam (or the smaller one of the probe and pump beam), which is about 5 mm in our case. The estimated broadening is 16 kHz.

The saturation intensity I_S is 3 μW/cm^2 for Sr $^1S_0 -^3 P_1$ transition. Estimated saturation broadening is 191 kHz at 2000 μW/cm^2.

Although the laser is collimated, residual curvature and misalignment could still cause some broadening. With a beam size about 5 mm, the residual curvature angle θ of our laser is estimated to be smaller than 10^{-4} rad [2]. This broadening is given by

$$\begin{aligned}\Delta f_D &= 2\sqrt{\ln 2}\sqrt{\frac{2k_BT}{m}}\frac{f_{\text{atom}}}{c}\\ \Delta f_{TD} &= \theta\Delta f_D,\end{aligned}$$

where f_{atom} is the frequency of the atomic transition, and Δf_D and Δf_{TD} are the Doppler broadening and transverse Doppler broadening respectively. This mechanism gives an inhomogeneous broadening of 90 kHz.

All together, the estimated broadening is about 600 kHz, dominated by collisional and power broadening. Our measurement about 800 kHz agrees with this estimation.

A.6 Eliminating Noise from Amplitude Modulation

When an EOM or AOM is used for light phase modulation or frequency modulation, amplitude modulation comes up as a side effect. For example, in EOM, only the light component whose polarization is parallel to certain axis of the EOM crystal can be efficiently modulated. If there is a polarizer after the EOM, the modulated light component and the less-modulated component may beat to each other, result in amplitude modulation. If the two beating components has constant intensity I_1 and I_2 respectively, the output will be

$$I(t) = I_1 + I_2 + 2\sqrt{I_1 I_2}\cos(\Delta\phi(t)),$$

where $\Delta\phi(t)$ is the phase difference between two laser components caused by phase modulation. Because of the square root term, even a very weak less-modulated light component (e.g. 10^{-4} of the total power) leads to a strong amplitude modulation (2%). Other reasons like multiple reflection between the ends of the crystal and partly blocked laser beam will also cause amplitude modulations. In PDH technique, amplitude modulation results in an offset of the error signal. Due to temperature

[2] Beam radius changes by less than 0.5 mm at a distance of 5 meter.

variation, acoustic vibration and drifting electronics, this offset can drift and change the locked frequency.

To reduce amplitude modulation, interference between polarization components should be avoided; laser beam never be blocked or distorted; direction and position of the EOM (also AOM) be finely tuned. To tune the EOM (or AOM) precisely, we can monitor the AC signal directly from PD2 (in figure 3.7) during alignment. When the EOM (or AOM) is not optimized, the modulation of the PD2 output is dominated by a component at the same frequency as that of the frequency modulation. By careful adjustment, such a modulation can be eliminated and only a second harmonic component is left.

Besides that, we can also reduce actively the influence of amplitude noise. In a PDH scheme, for example, a second photo detector can be used to detect part of the light before it goes to the cavity [3]. This signal could be used as a background reference. The error signal offset coming from it will be subtracted from the usual error signal. Another way [16] of using the signal from the reference PD is to stabilize the light power with an AOM.

[3] In spectroscopy, PD2 in figure 3.7 does the job.

Bibliography

[1] T. Akatsuka, M. Takamoto, and H. Katori, Nature Phys. **4**, 954 (2008)

[2] G. K. Campbell, A. D. Ludlow, S. Blatt, J. W. Thomsen, M. J. Martin, M. H. G. de Miranda, T. Zelevinsky, M. M. Boyd, J. Ye, S. A. Diddams, T. P. Heavner, T. E. Parker, and S. R. Jefferts, Metrologia **45**, 539 (2008)

[3] A. J. Daley, M. M. Boyd, J. Ye, and P. Zoller, Phys. Rev. Lett. **101**, 170504 (2008)

[4] A. V. Gorshkov, A. M. Rey, A. J. Daley, M. M. Boyd, J. Ye, P. Zoller, and M. D. Lukin, Phys. Rev. Lett. **102**, 110503 (2009)

[5] M. Hermele, V. Gurarie, and A. M. Rey, Phys. Rev. Lett. **103**, 135301 (2009)

[6] R. Ciurylo, E. Tiesinga, S. Kotochigova, and P. S. Julienne, Phys. Rev. A **70**, 062710 (2004)

[7] C. P. Koch, Phys. Rev. A **78**, 063411 (2008)

[8] S. Stellmer, M. K. Tey, B. Huang, R. Grimm, and F. Schreck, Phys. Rev. Lett. **103**, 200401 (2009)

[9] F. Sorrentino, G. Ferrari, N. Poli, R. Drullinger, and G. M. Tino, Mod. Phys. Lett. B **20**, 1287 (2006)

[10] S. Kraft, F. Vogt, O. Appel, F. Riehle, and U. Sterr, Phys. Rev. Lett. **103**, 130401 (2009)

[11] T. Fukuhara, S. Sugawa, and Y. Takahashi, Phys. Rev. A **76**, 051604 (2007)

[12] B. DeMarco and D. S. Jin, Science **285**, 1703 (1999)

[13] B. E. C. Saleh and M. C. Teich, *Fundamentals of Photonics*, 2nd ed. (John Wiley & Sons, Inc., Hoboken, New Jersey, 2007)

[14] E. Kapon, *Semiconductor Lasers I, Fundamentals*, Vol. I (Academic Press, San Diego, 1999)

[15] C. E. Wieman and L. Hollberg, Rev. Sci. Instrum. **62** (1991)

[16] J. Alnis, A. Matveev, N. Kolachevsky, T. Udem, and T. W. Hänsch, Phys. Rev. A **77**, 053809 (2008)

[17] C. J. Hawthorn, K. P. Weber, and R. E. Scholtena, Rev. Sci. Instrum. **72**, 4477 (2001)

[18] A. E. Siegman, *Lasers* (University Science Books, 1986)

[19] J. C. Bienfang, R. F. Teehan, and C. A. Denman, Rev. Sci. Instrum. **72**, 3208 (2001)

[20] M. D. Harvey and A. G. White, Opt. Commun. **221**, 163 (2003)

[21] R. W. P. Drever, J. L. Hall, F. V. Kowalski, J. Hough, G. M. Ford, A. J. Munley, and H. Ward, Appl. Phys. B **31**, 97 (1983)

[22] E. D. Black, Am. J. Phys. **69**, 79 (2001)

[23] G. F. Franklin, J. D. Powell, and A. Emami-Naeini, *Feedback Control of Dynamic Systems*, 4th ed. (Prentice Hall, 2002)

[24] J. R. Leigh, *Control Theory* (The Institute of Electrical Engineers, London, 2004)

[25] J. Bechhoefer, Rev. Mod. Phys. **77**, 783 (2005)

[26] R. Lang and K. Kobayashi, IEEE J. Quantum Electron. **16**, 347 (1980)

[27] H. Li and H. Telle, IEEE J. Quantum Electron. **25**, 257 (1989)

[28] P. Laurent, A. Clairon, and C. Breant, IEEE J. Quantum Electron. **25**, 1131 (1989)

[29] D. S. Elliott, R. Roy, and S. J. Smith, Phys. Rev. A **26**, 12 (1982)

[30] N. Poli, G. Ferrari, M. Prevedelli, F. Sorrentino, R. Drullinger, and G. Tino, Spectrochim. Acta Part A **63**, 981 (2006)

[31] M. ASANO and K. KUBO, J.Nucl.Sci.Technol. **15**, 765 (1978)

[32] T. Kurosu and F. Shimizu, Jpn. J. Appl. Phys. **29**, L2127 (1990)

[33] T. Ido and H. Katori, Phys. Rev. Lett. **91**, 053001 (2003)

[34] M. M. Boyd, A. D. Ludlow, S. Blatt, S. M. Foreman, T. Ido, T. Zelevinsky, and J. Ye, Phys. Rev. Lett. **98**, 083002 (2007)

[35] P. Lemonde, Eur. Phys. J. Special Topics **172**, 81 (2009)

[36] A. V. Gorshkov, M. Hermele, V. Gurarie, C. Xu, P. S. Julienne, J. Ye, P. Zoller, E. Demler, M. D. Lukin, and A. M. Rey, arXiv:0909.2610(2009)

[37] R. Ciuryło, E. Tiesinga, S. Kotochigova, and P. S. Julienne, Phys. Rev. A **70**, 062710 (2004)

[38] S. Kotochigova, T. Zelevinsky, and J. Ye, Phys. Rev. A **79**, 012504 (2009)

[39] T. C. Killian, T. Pattard, T. Pohl, and J. M. Rost, Phys. Rep. **449**, 77 (2007)

[40] R. Grimm, M. Weidemüller, and Y. B. Ovchinnikov, Adv. At. Mol. Opt. Phys. **42**, 95 (2000)

[41] C. Chin, R. Grimm, P. Julienne, and E. Tiesinga, Rev. Mod. Phys.(2009), in press; arXiv:0812.1496

[42] Y. Takasu, K. Maki, K. Komori, T. Takano, K. Honda, M. Kumakura, T. Yabuzaki, and Y. Takahashi, Phys. Rev. Lett. **91**, 040404 (2003)

[43] T. Fukuhara, Y. Takasu, M. Kumakura, and Y. Takahashi, Phys. Rev. Lett. **98**, 030401 (2007)

[44] T. Fukuhara, S. Sugawa, Y. Takasu, and Y. Takahashi, Phys. Rev. A **79**, 021601(R) (2009)

[45] H. Katori, T. Ido, Y. Isoya, and M. Kuwata-Gonokami, in *Atomic Physics 17*, edited by E. Arimondo, P. DeNatale, and M. Inguscio (American Institute of Physics, Woodbury, 2001) pp. 382–396

[46] G. Ferrari, R. E. Drullinger, N. Poli, F. Sorrentino, and G. M. Tino, Phys. Rev. A **73**, 023408 (2006)

[47] Y. N. Martinez de Escobar, P. G. Mickelson, M. Yan, and T. C. Killian, arXiv:0906.1837(2009)

[48] J. Ye, private communication

[49] R. Ciuryło, private communication

[50] A. Stein, H. Knöckel, and E. Tiemann, Phys. Rev. A **78**, 042508 (2008)

[51] Y. N. Martinez de Escobar, P. G. Mickelson, P. Pellegrini, S. B. Nagel, A. Traverso, M. Yan, R. Côté, and T. C. Killian, Phys. Rev. A **78**, 062708 (2008)

[52] T. Loftus, J. R. Bochinski, and T. W. Mossberg, Phys. Rev. A **66**, 013411 (2002)

[53] X. Xu, T. H. Loftus, J. L. Hall, A. Gallagher, and J. Ye, J. Opt. Soc. Am. B **20**, 968 (2003)

[54] S. B. Nagel, C. E. Simien, S. Laha, P. Gupta, V. S. Ashoka, and T. C. Killian, Phys. Rev. A **67**, 011401(R) (2003)

[55] A. Traverso, R. Chakraborty, Y. N. Martinez de Escobar, P. G. Mickelson, S. B. Nagel, M. Yan, and T. C. Killian, Phys. Rev. A **79**, 060702(R) (2009)

[56] P. G. Mickelson, Y. N. Martinez de Escobar, P. Anzel, B. J. DeSalvo, S. B. Nagel, A. J. Traverso, M. Yan, and T. C. Killian, arXiv:0907.2270(2009)

[57] A. Griesmaier, J. Werner, S. Hensler, J. Stuhler, and T. Pfau, Phys. Rev. Lett. **94**, 160401 (2005)

[58] H. Katori, T. Ido, Y. Isoya, and M. Kuwata-Gonokami, Phys. Rev. Lett. **82**, 1116 (1999)

[59] M. H. Anderson, J. R. Ensher, M. R. Matthews, C. E. Wieman, and E. A. Cornell, Science **269**, 198 (1995)

[60] *Bose-Einstein condensation in atomic gases*, edited by M. Inguscio, S. Stringari, and C. Wieman (North Holland, Amsterdam, 1999) Proceedings of the International School of Physics "Enrico Fermi", Course CXL, Varenna, 7-17 July 1998

[61] T. Fukuhara, S. Sugawa, M. Sugimoto, S. Taie, and Y. Takahashi, Phys. Rev. A **79**, 041604(R) (2009)

[62] N. Nemitz, F. Baumer, F. Münchow, S. Tassy, and A. Görlitz, Phys. Rev. A **79**, 061403 (2009)

[63] M. D. Barrett, J. A. Sauer, and M. S. Chapman, Phys. Rev. Lett. **87**, 010404 (2001)

[64] G. Cennini, G. Ritt, C. Geckeler, and M. Weitz, Appl. Phys. B **77** (2003)

[65] T. Kinoshita, T. Wenger, and D. S. Weiss, Phys. Rev. A **71**, 011602(R) (2005)

[66] *Cold Molecules: Theory, Experiment, Applications*, edited by R. V. Krems, B. Friedrich, and W. C. Stwalley (Taylor & Francis, 2009)

[67] J. K. Crane, M. J. Shaw, and R. W. Presta, Phys. Rev. A **49**, 1666 (1994)